GEORG-AUGUST-UNIVERSITÄT
GÖTTINGEN

Fakultät für
Physik

Master's Thesis

Entwicklung neuer Trigger für die ATLAS Run 2 Suche nach dem Higgs Boson, produziert via Vektorboson-Fusion, und zerfallend in ein Beauty-Quark-Paar

Development of new triggers for the ATLAS Run 2 search for the Higgs boson produced in vector boson fusion and decaying into a pair of beauty quarks

prepared by

Fabian Kukuck

from Henstedt-Ulzburg

at the II. Physikalischen Institut, and
SLAC National Accelerator Laboratory

Thesis number: II.Physik-UniGö-MSc-2016/08

Thesis period: 7th September 2016 until 28th February 2017

First referee: Prof. Dr. Arnulf Quadt

Second referee: Prof. Ariel Schwartzman

Contents

1. Introduction

The Standard Model of Elementary Particle Physics (SM) has been very successful in describing the fundamental building blocks of the universe. The Higgs boson was the last particle missing to experimentally confirm the SM particle zoo. After about 40 years of search at various experiments, it has been found in 2012 at the Large Hadron Collider (LHC) at CERN. Its properties are now under detailed scrutiny and yet to be observed is its production in the vector boson fusion channel. The goal of this thesis is to introduce new triggers that aid the ATLAS Run 2 search of the Standard Model Higgs boson produced in such a channel and subsequently decaying to a pair of b-quarks. Chapter 2 provides an overview of the SM, and Chapter 3 presents a short summary of the history of the discussed search. Chapter 4 describes the ATLAS experiment at the Large Hadron Collider, the experiment within this thesis is written. Chapter 5 introduces new triggers for the search that were developed within this thesis. Finally, Chapter 6 gives an outlook onto future developments and conclusions on what to expect from the ATLAS Run 2 search.

2. Theoretical Framework

2.1. The Standard Model

The SM successfully describes elementary particles and their interactions. It was formulated in the 1960s and 1970s and consists of the Glashow-Weinberg-Salam (GWS) model of electroweak (EW) interactions (describing electromagnetic and weak forces [1–3]) and Quantum Chromodynamics (QCD; describing the strong force [4–6]). Since then, the predictions made by the SM were tested in many dedicated experiments and until now are found to be valid with only a few exceptions.[1] This makes the SM one of the most successful theories in physics.

The SM divides the particle spectrum into fermions (half integer spin) and bosons (integer spin). Gauge bosons are the mediators of the fundamental forces:[2] the photon (γ) is the mediator of the electromagnetic interaction, the $W^{\pm}$ and Z bosons of the weak interaction, and the gluon (g) of the strong interaction.
While the photon is massless and carries no electromagnetic charge, the W and Z bosons are very heavy ($\mathcal{O}(100\,\mathrm{GeV})^3$) in comparison with other elementary particles and the $W^{\pm}$ carry an electromagnetic charge of $\pm e$. Gluons are massless and electrically neutral, but carry color charges.
Fermionic elementary particles are divided into *Leptons* and *Quarks*. They are sorted into weak isospin (the "charge" of the weak interaction) doublets. The group of leptons consists of the isospin-down (*down-type*) and electrically charged particles electron e^-, muon μ^-, and tau lepton τ^-, and their corresponding isospin-up (*up-type*) partners, the electrically neutral neutrinos ν_e, ν_μ, and ν_τ. The group

[1] Exceptions are for example neutrino masses/oscillations, or the nature of dark matter.
[2] Excluding gravitation.
[3] Throughout this thesis, natural units with $c = 1$ and $\hbar = 1$ are used.

of quarks consists of the up-type quarks up u, charm c, and top t (electric charge $+2/3$), paired with the down-type quarks down d, strange s, and beauty (or bottom) b (electric charge $-1/3$). All quarks carry a color charge. Additionally, all particles have antiparticles which are the charge conjugates of their particles. Furthermore, the mentioned fermions are categorized into three generations, as shown in Tab. 2.1. Generations of quarks and leptons differ only in mass from other generations of the respective fermion type. Fermions of generation 1 are the lightest, and the masses increase with generation.

	Matter			Bosons
	Gen. 1	Gen. 2	Gen. 3	γ
quarks	u	c	t	W^-
	d	s	b	Z
leptons	ν_e	ν_μ	ν_τ	g
	e^-	μ^-	τ^-	H

Table 2.1.: Particles of the Standard Model. All particles have antiparticles and all bosons but the W^- are their own antiparticles.

The SM is a quantum field theory that models particle interactions via the symmetry (invariance under transformation) group $SU(3)_C \times SU(2)_I \times U(1)_Y$. Here, $SU(3)_C$ is the color (C) symmetry of the strong interaction, $SU(2)_I$ is the weak isospin (I) symmetry, and $U(1)_Y$ is the hypercharge (Y) symmetry. The SM is based on a Lagrangian density with all particle masses set to zero to ensure invariance under all the transformations of the underlying group. In a non-explicit form, the Lagrangian of the SM can be written as

$$\begin{aligned}\mathscr{L}_{\text{SM}} &= \mathscr{L}_{SU(3)_C} + \mathscr{L}_{SU(2)_I \times U(1)_Y} \\ &= \underbrace{\mathscr{L}^{\text{Gauge}}_{SU(3)_C} + \mathscr{L}^{\text{Matter}}_{SU(3)_C}}_{\text{QCD}} + \underbrace{\mathscr{L}^{\text{Gauge}}_{SU(2)_I \times U(1)_Y} + \mathscr{L}^{\text{Matter}}_{SU(2)_I \times U(1)_Y} + \mathscr{L}^{\text{Higgs}}_{SU(2)_I \times U(1)_Y} + \mathscr{L}^{\text{Yukawa}}_{SU(2)_I \times U(1)_Y}}_{\text{EW}}.\end{aligned}$$

In this formulation, the $\mathscr{L}^{\text{Gauge}}$ terms describe the dynamics of the gauge fields

(QCD: gluons; EW: W, Z, and γ), and the $\mathscr{L}^{\text{Matter}}$ terms model the interaction of particles with those gauge fields. All fields in these two terms are massless and adding a traditional mass term would spoil the local gauge invariance of the theory. Brout, Englert and Higgs (BEH) proposed in 1964 [7, 8] a mechanism to give mass to the bosons that preserves the gauge symmetry. Within the BEH mechanism all massive particles acquire mass via an interaction with the Higgs field, described in $\mathscr{L}^{\text{Higgs}}_{SU(2)_I \times U(1)_Y}$ for the heavy gauge bosons, and in $\mathscr{L}^{\text{Yukawa}}_{SU(2)_I \times U(1)_Y}$ for the fermions, where the mass is proportional to the interaction strength (*Yukawa coupling*). As a consequence of the Higgs field, the BEH mechanism implies the existence of a *massive* scalar boson, referred to as the Higgs boson H.

2.2. Standard Model Higgs Boson H

2.2.1. Brout-Englert-Higgs Mechanism

The BEH mechanism is used in the SM to introduce masses to the massless particles in $\mathscr{L}^{\text{Gauge}}$ and $\mathscr{L}^{\text{Matter}}$. Within it, *spontaneous symmetry breaking* from $SU(3)_C \times SU(2)_I \times U(1)_Y$ to $SU(3)_C \times U(1)_Q$ (where Q is the charge symmetry of the electromagnetic interaction) leaves the photon and gluon massless while providing masses to the weak bosons. The symmetry breaking is achieved by introducing the Higgs field

$$\phi = \begin{pmatrix} \phi^+ \\ \phi^0 \end{pmatrix},$$

an isospin doublet of complex scalar fields. This scalar particle ϕ can be described by the Lagrangian

$$\mathscr{L}^{\text{Higgs}}_{SU(2)_I \times U(1)_Y} = (D_\mu \phi)^\dagger (D^\mu \phi) \underbrace{-\mu^2(\phi^\dagger \phi) - \lambda(\phi^\dagger \phi)^2}_{-V(\phi)}, \tag{2.1}$$

where D is the *covariant derivative* containing the four gauge fields $W^{(1)}$, $W^{(2)}$, $W^{(3)}$, and B that describe the W and Z bosons, and $\mu, \lambda \in \mathbb{R}$.
Demanding the model to be physical it is required for the Lagrangian to have a

finite minimum ("ground state"), and hence λ is set to $\lambda > 0$. Now, the non-trivial postulate is made that the vacuum expectation value (VEV) of the field—the field present when no excitations take place—is non zero. For this, μ^2 is set to $\mu^2 < 0$. The potential $V(\phi)$ now has a form which is commonly referred to as the "Mexican hat potential." This potential has an infinite set of minima on the circle with radius

$$\sqrt{\frac{-\mu^2}{2\lambda}} =: v.$$

The non-zero VEV ϕ_0 will in nature be realized by a certain *fixed* point on this circle, spoiling the symmetry that the Lagrangian possessed (spontaneous symmetry breaking). Without loss of generality

$$\phi_0 := \langle 0|\phi|0\rangle = \begin{pmatrix} 0 \\ v/\sqrt{2} \end{pmatrix}$$

is chosen. It is > 0 just in the neutral dimension because in case the VEV would be charged, photons would be observed interacting with the vacuum. After applying a local gauge transformation[4] referred to as the unitary gauge, the resulting Lagrangian is referred to as the GWS model. The four physical gauge bosons of this Lagrangian (= the four bosons of the electroweak interaction) are found to be

$$\begin{aligned} W_\mu^\pm &= (W_\mu^{(1)} \mp i W_\mu^{(2)})/\sqrt{2} && \text{with} \quad m_W = \frac{1}{2} g_\mathrm{W} v, \\ Z_\mu &= -\sin\theta_\mathrm{W} B_\mu + \cos\theta_\mathrm{W} W_\mu^{(3)} && \text{with} \quad m_Z = \frac{1}{2}\frac{g_\mathrm{W}}{\cos\theta_\mathrm{W}} v, \\ A_\mu &= \cos\theta_\mathrm{W} B_\mu + \sin\theta_\mathrm{W} W_\mu^{(3)} && \text{with} \quad m_A = 0, \end{aligned}$$

where $\tan\theta_\mathrm{W} := g'/g_\mathrm{W}$, while g_W being the coupling of the $\mathrm{SU}(2)_I$ gauge interaction, and g' being one factor of the coupling of the $\mathrm{U}(1)_Y$ interaction (the other is $Y/2$).

The breaking of the symmetry provides mass terms for the three massive gauge bosons of the electroweak interaction, and leaves the photon massless. However, it is unavoidable to require the excitation of the Higgs field to be realized in nature,

[4] Since the Lagrangian was built to be local gauge invariant, the physics is not changed by this.

a *massive* neutral scalar boson referred to as the Higgs boson H.
The Higgs field can also be used to create mass terms for the fermions. Here, the fermion fields couple directly to the Higgs field via Yukawa coupling terms (in $\mathscr{L}^{\text{Yukawa}}_{SU(2)_I \times U(1)_Y}$) and the strength of a respective Yukawa coupling determines the mass of a respective fermion.

2.2.2. Higgs Boson Production Modes

The main production modes of the SM Higgs boson (in what follows simply Higgs boson) at the LHC (Sec. 4.1) are gluon gluon fusion (ggF or GF), vector boson fusion (VBF), associated production with a vector boson (VH), and associated production with a top quark pair (ttH). Fig. 2.1 shows the leading order Feynman diagrams for these production modes. Each production mode has different

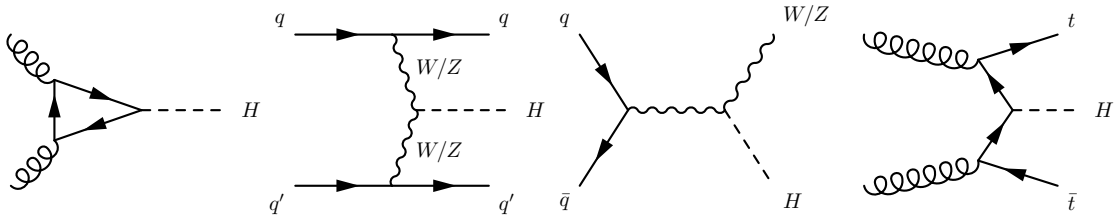

Figure 2.1.: Leading order Higgs boson main production modes at the LHC. From left to right: ggF, VBF, VH, and ttH.

properties, which are briefly illustrated in this section. All predicted Higgs boson production cross sections are given for a mass of $m_H = 125\,\text{GeV}$ and 13 TeV center-of-mass energy.

ggF The gluon gluon fusion process is the most prominent at the LHC, with a predicted cross section of about 48.6 pb [9].[5]

VBF The vector boson fusion production channel has a cross section of 3.78 pb [9]. The event signature features a high p_T Higgs boson, and two high energy jets (see Sec. 2.4.6) that result from the quarks that emit the fusing vector bosons.

[5] Compared to for example a predicted $t\bar{t}$ cross section of around 800 pb [10] for a top quark mass of 173.2 GeV and 13 TeV center of mass energy the Higgs boson production cross sections are rather low.

Since these are radiations of virtual vector bosons, the recoil of the quarks is only very light. This leads to only slight deflections of the quarks from the beam axis, and thus the expectation of one or more jets in the forward direction. Additionally, due to the nature of the electroweak interaction, no QCD color exchange occurs. As a result, the quarks that radiated the vector bosons are color connected to the proton remnants. The VBF production channel is addressed in this thesis.

VH With a cross section of about 2.26 pb [9], this production mode, which is also referred to as *Higgsstrahlung*, includes the production of an additional vector boson (W or Z) alongside the Higgs boson. The final states depend on the produced vector boson and its decay mode. Hadronically decaying W and Z bosons are usually not considered for an analysis, since they are harder to distinguish from QCD multijet events. For leptonically decaying W bosons an isolated lepton and missing transverse energy (MET) due to the neutrino is expected (see Sec. 2.4.6). Z bosons are considered for analysis in their $\ell\ell$[6] and $\nu\nu$ decay channels, expecting two isolated leptons boosted in the same direction in the former, or a large amount of MET in the latter case.

ttH The cross section of the Higgs boson production with an associated $t\bar{t}$-pair has a cross section of about 0.51 pb [9]. This production mode allows for a direct measurement of the Yukawa coupling of the top quark, which the other modes are only sensitive to through loop effects. The final states depend on the top-pair decay mode: dileptonic, semileptonic, or all-hadronic. The b-jets from the top quark decays[7] help to distinguish these events from background (see Sec. 2.4.6.3). While the all-hadronic decay channel is difficult to distinguish from QCD multijet events, the dileptonic and semileptonic decay modes (with electrons and muons) provide better handles to identify ttH events. Here, alongside the respective one or two leptons, MET is expected in the final state.

[6] ℓ refers to either e or μ.
[7] Top quarks almost exclusively decay into W^+b.

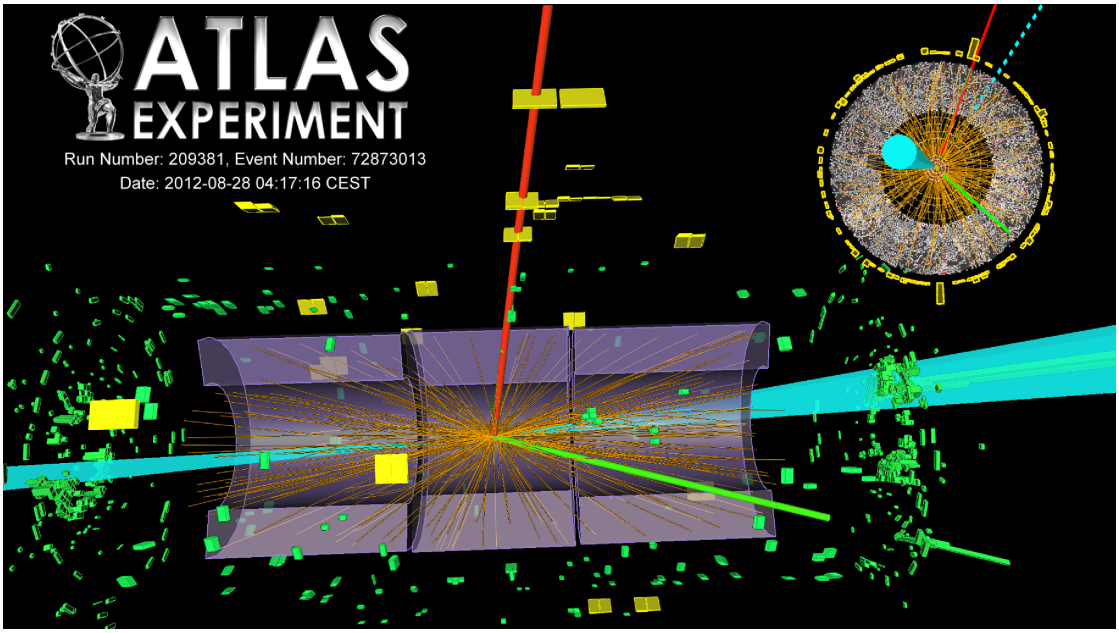

Figure 2.2.: Exemplary VBF event recorded with the ATLAS detector. $H \to \tau\tau \to e\mu + E_T^{\text{miss}}$ is shown. In red the muon path, and in green the electron path. Also, two jets with a large pseudorapidity gap between each other are illustrated (turquoise cones). The illustration is taken from Ref. [11].

2.2.3. Higgs Boson Decay Modes

The SM does not predict the Higgs boson's mass, but due to various theoretical constraints its mass is constrained to be $\lesssim 1000\,\text{GeV}$. Due to its nature the Higgs boson can, in principle, decay to all massive SM particles (Fig. 2.4a). The SM predicts the couplings to the various particles to be proportional to the respective masses of the decay products. It thus favors decays into high mass particles. It cannot directly decay into photons or gluons but only via higher order loops (Fig. 2.4b). Fig. 2.3 shows the predicted branching ratios of the Higgs boson for different Higgs boson masses. In the recent years, the Higgs boson was experimentally found and its mass determined to be $125.7 \pm 0.4\,\text{GeV}$ [12]. This mass—which falls in the region referred to as the intermediate mass region—results in an interesting decay behavior where many decay channels are experimentally relevant. Decays where the decay products' total rest mass exceeds the Higgs boson rest mass, e. g. $H \to t\bar{t}$, are kinematically suppressed. However, since the coupling to

vector bosons is approximately one order of magnitude higher than to fermions [12], the decays $H \to WW^*$ and $H \to ZZ^*$ are still among the usual decay modes of the Higgs boson. SM predictions for the branching ratios at $m_H = 125\,\text{GeV}$ are [12]:

$$\begin{aligned} H &\to b\bar{b} && (57.7^{+1.9}_{-1.9})\,\%, \\ H &\to WW^* && (21.5^{+1.0}_{-0.9})\,\%, \\ H &\to \tau^+\tau^- && (6.3^{+0.4}_{-0.4})\,\%, \\ H &\to ZZ^* && (2.6^{+0.2}_{-0.1})\,\%, \\ H &\to \gamma\gamma && (0.23^{+0.01}_{-0.01})\,\%. \end{aligned}$$

The decay into a pair of beauty quarks is the most common decay channel. Since an observation here is yet to be made, this large decay channel is still open to physics beyond the SM.

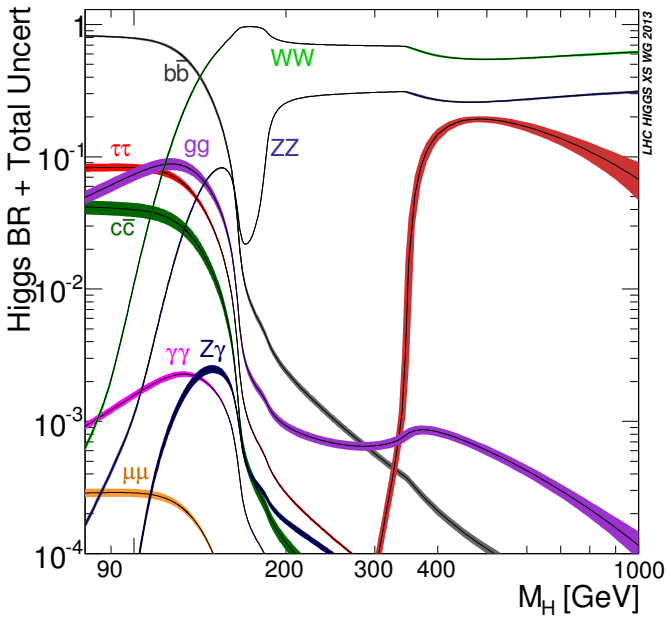

Figure 2.3.: Standard Model Higgs boson decay branching ratios and their uncertainties. The figure is taken from Ref. [13].

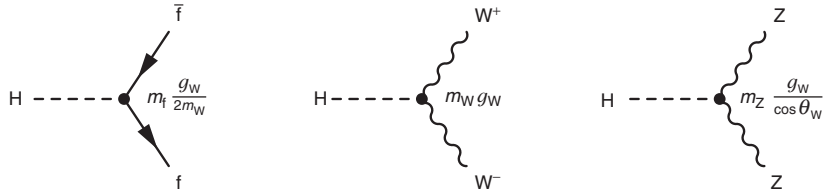

(a) LO decays to fermions and massive bosons. The coupling strengths are indicated.

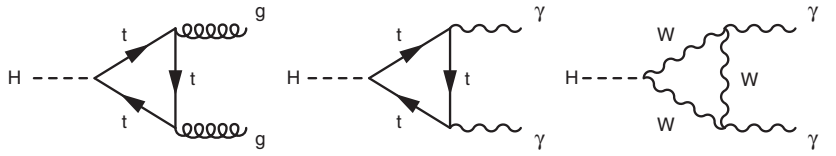

(b) NLO decays through loop diagrams.

Figure 2.4.: SM Higgs boson's main decay modes. The figures are taken from Ref. [14].

2.3. Phenomenology of QCD

2.3.1. Color Confinement

Quantum Chromodynamics is the theory that describes the strong interactions among gluons and quarks. Since gluons are self interacting, the loop-corrections that have to be applied to the strong coupling constant lead to an interesting behavior of the strong force: its strength is inversely proportional to the relevant energy scale (or, equivalently, proportional to distance). This phenomenon is referred to as *asymptotic freedom* and results in a vanishing force as the energy scale approaches infinity, and in an infinitely strong force towards low energies. An implication of this is that quarks only exist in compound states, never free (*color confinement*). The known compound states (hadrons and antihadrons) are all color neutral and grouped into mesons (quark-antiquark) and baryons (three quarks).[8] Quarks are not color neutral and therefore exchange gluons. These gluons in turn act on each other via gluons and thus a *QCD string* develops between quark pairs (Lund string model). When quarks are separated from each other

[8]Recently, experimental results have been reported that are consistent with the observation of tetraquark (four quarks) and pentaquark states (five quarks) [15, 16].

and the string elongates, it eventually becomes energetically favorable to create a new $q\bar{q}$-pair from the vacuum, rather than maintaining the string between them. To this new pair, the same phenomenon applies and further hadrons are created (*hadronization*). Macroscopically, this causes the formation of *jets* that consist of many hadrons.

2.3.2. Parton Distribution Functions

Being compound particles, hadrons do not collide with each other as a whole, but rather their *partons* interact with each other upon collision. The proton consists of *valence* quarks (two u-quarks, one d-quark), and gluons that exert forces on the valence quarks and keep them in a bound state. Additionally, a gluon can split into a virtual $q\bar{q}$-pair and recombine again. These virtual quarks, referred to as *sea* quarks, can participate in collisions in the same way as valence quarks can. At hadron colliders, the center-of-mass energy $\sqrt{s}$ is the upper bound on the energy a collision can occur with. The actual energy with that two partons collide is usually lower and unknown event-by-event. *Parton Distribution Functions* (PDFs) [17] are an approach to make statistical statements about the collision energy of two partons. A PDF, exemplarily shown in Fig. 2.5, gives a parametrization of the probability that a particular parton from the hadron will be found at an energy fraction x of the hadron at some momentum scale Q^2. PDFs are used for cross-section calculations where it is averaged over possible input partons and energy fractions.

2.4. Reconstruction and Identification of Particles

Since the Big Bang, the universe has "cooled down" to significantly lower energy densities. As a result, most of the SM particles are not usually present in the environment. In order to induce nature to create particles of higher masses, it usually takes high energy densities, which are for example naturally produced through cosmic rays in the upper layers of Earth's atmosphere, or nowadays also artificially by particle accelerators. The latter allow to build experiments where two high

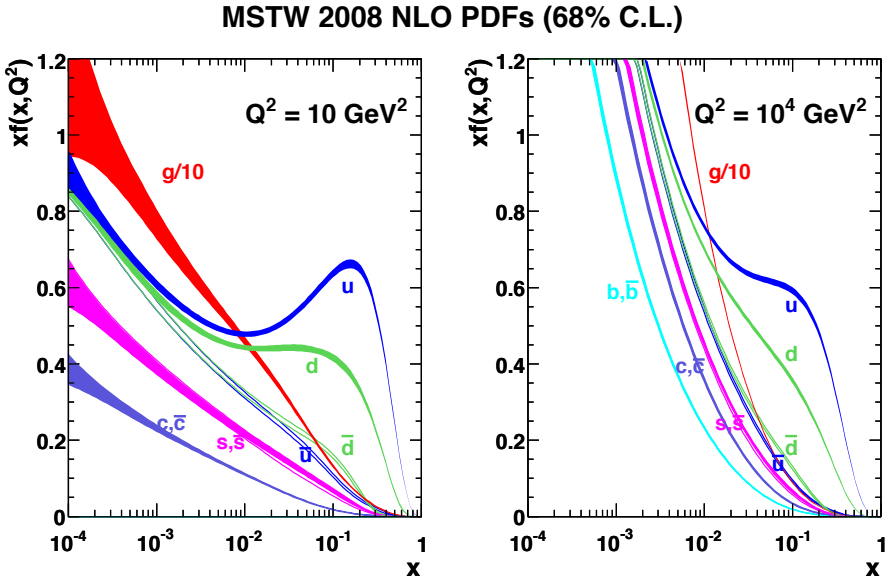

Figure 2.5.: Exemplary PDF set. It can be used to calculate the probability that a parton in a hadron will posses the energy fraction x, dependent on a momentum scale Q^2. The figure is taken from Ref. [18].

momentum particles collide with each other (collider experiments). In a collision event (or just *event*) highly energy dense environments are created, where other particles can form in. Apart from electrons, neutrinos, photons, protons and bound neutrons, all other SM particles have finite lifetimes and decay into other particles. Usually these lifetimes are so short that it is not possible to build a detector close enough to a created particle to detect it directly. Consequently, only the decay products can be measured. The act of measurement inherently requires the particles to interact with the detector. For different particles, different measurement techniques have been developed that exploit their behavior when interacting with matter. A comprehensive description of these ways of measurement is beyond the scope of this thesis, and they will only be touched on briefly in the following.

2.4.1. Electrons and Photons

These particles go through complementary processes enabling them to be measured. Highly energetic photons undergo the process of pair-production, where a photon converts into an e^+e^--pair. In the presence of charged particles (e. g.

atomic nuclei), electrons and positrons (e^+) experience deflection and deceleration, whereby a photon is emitted, to conserve energy. This process is referred to as *bremsstrahlung*. Pair-production and bremsstrahlung occur in an alternating fashion, creating what is referred to as an electromagnetic shower. As more and more particles are created, their individual kinetic energy decreases. Photons eventually fall under the pair-production threshold, and other processes of energy loss become relevant for electrons and positrons. The energy of the particles can be measured via Cherenkov radiation and the photoelectric effect. Electromagnetic calorimeters (ECals) are used to induce electromagnetic showers and measure their energy.

2.4.2. Muons

Muons are exceptional in such a way that their average lifetime ($\tau_\mu = 2.2 \times 10^{-6}\,\mathrm{s}$ [12]) is long enough to travel macroscopic distances and they can thus be detected directly. As muons are 200 times heavier than electrons, they do not radiate bremsstrahlung and thus do not produce showers. They are usually measured via ionization in the outermost regions of detectors, because they are the only charged particles that reach these parts.

2.4.3. Neutrinos

As neutrinos only interact weakly, they are practically impossible to measure directly. Their creation can only be inferred by measuring the difference between collision energy of the initial state particles and total detected energy of the decay products (assuming conservation of energy). In hadron colliders, compound particles collide, and the initial energy of the partons is not measurable. As a result, only the missing *transverse* energy (MET) of the event can be inferred (assuming the particles collide with only longitudinal momentum).

2.4.4. Taus

With a mean lifetime of $\tau_\tau = (290.3 \pm 0.5) \times 10^{-15}\,\mathrm{s}$ [12], τ leptons are not directly observable. They can decay leptonically or hadronically, leaving distinct signatures

like a lepton, a jet with photons, or three collimated jets in the detector. They are always accompanied by MET, since a ν_τ is always produced in τ decays.

2.4.5. Heavy Bosons

The heavy bosons W, Z, and H all have lifetimes under 10^{-21} s (calculable from the measured or predicted decay widths [12]). The Z, and H bosons decay into pairs of particle and antiparticle. The W boson can decay leptonically (then accompanied by MET), or hadronically. The system of the decay products has an invariant mass corresponding to the mass of the mother particle. Because the masses of these heavy bosons, particularly m_Z and m_W, are well known nowadays, their identification can be relatively straight forward in some decay channels (a very prominent example is $Z \to \mu^+\mu^-$).

2.4.6. Jets

As already indicated in Sec. 2.3.1, quarks and gluons, both color charged, are color confined and thus cannot be observed in separation. They always form color neutral mesons and baryons that, in accumulation, form showers of particles referred to as jets. These are detected in ECals and hadronic calorimeters (HCals) that measure their energy based on ionization and Cherenkov radiation. Much information about the particles that initiated the jets is lost and the goal of *jet reconstruction* is to infer as much as possible about those particles. This section provides an overview of the topic.

2.4.6.1. The Anti-k_T Jet Algorithm

Since jets are so abundantly produced at hadron colliders, they often overlap in the detector. For this reason, it is not trivial to assign energy deposits in the calorimeters and tracks in the pixel detector to specific jets, not by eye, neither programmatic. *Jet algorithms* are used in order to reconstruct jets from various objects. They read input 4-momenta and build output 4-momenta, and are thus usable at any stage of perturbation theory, be it simulated parton or hadron level events, or data from detector objects.

Within the ATLAS experiment, the anti-k_T algorithm [19] is utilized for jet reconstruction, which is a *sequential recombination algorithm*. These types of algorithms use a distance metric to cluster together pairs of particles whose "distance" is below some threshold. The distance metric of the anti-k_T algorithm uses the quantities

$$d_{ij} = \min\left(1/p_{Ti}^2, 1/p_{Tj}^2\right)\frac{\Delta R_{ij}^2}{R^2}, \qquad \Delta R_{ij}^2 = (y_i - y_j)^2 + (\phi_i - \phi_j)^2,$$
$$d_{iB} = 1/p_{Ti}^2,$$

where y_i is the rapidity of particle i, and R is referred to as the *distance parameter*. The algorithm proceeds as follows

1. Between all pairs of particles ij, calculate d_{ij} and d_{iB}.
2. Find the minimum of all d_{ij} and d_{iB}.
3. If that minimum is a d_{ij}, combine i and j into a single particle and return to step 1. Else, it is a d_{iB}, and then i is declared a final jet and removed from the particle list.
4. Terminate when the particle list is empty.

The distance parameter R is a chosen parameter and determines the size of the created jets. With the anti-k_T algorithm, soft particles are always clustered with high energy ones before they can cluster among themselves. This is why jets in this algorithm grow outwards from "hard seeds," and form circular jets.[9] A common distance parameter used by the ATLAS collaboration is $R = 0.4$, a size that is large enough to cover most of the radiation of a typical parton shower, and small enough to keep overlaps limited.

2.4.6.2. Jet Inputs

Many different objects can serve as input to a jet algorithm, and it depends on the problem which ones are chosen. For example, clustering simulated Monte Carlo particles would result in jets referred to as *truth jets*; jets reclustered from tracks

[9] Among experimentalists this is a desired behavior.

in the vertex detector are *trackjets*; and *calorimeter jets* are formed out of energy deposits in the calorimeters. The measurement of the energy of latter jets is, after applying calibrations, roughly at the same scale as the quarks that initiated them (e. g. the invariant mass of a dijet system that emerged from a Z boson would peak at m_Z).
A widely used input for the anti-k_T algorithm at the ATLAS experiment are *topoclusters* [20]. These are attained by merging in a specific manner the calorimeter cells (which are the smallest entities in a calorimeter) to "three dimensional topological clusters" (topoclusters). Using those as input, instead of directly the cells, reduces the impact of some issues that come with the cells, e. g. their noisiness and great number. The merging methods are conceived to produce approximately one cluster per particle that interacted with the calorimeter. The clusters are also calibrated according to some scale, typically the electromagnetic (EM) scale or the fully calibrated scale. Former reconstructs the energy deposits of photons and electrons correctly. However, it does not apply measures to compensate for the generally smaller energy signals for hadrons in the ATLAS calorimeter (*non-compensating*, see Sec. 4.2.3), for signal losses due to noise suppression, or for signal losses due to inactive material between the calorimeter modules. These are accounted for by the fully calibrated scale.
From these input clusters the anti-k_T algorithm calculates, in the case of EM calibration and $R = 0.4$, jets that are referred to as `AntiKt4EMTopoJets`. Typically, an analysis will be performed on `AntiKt4EMTopoJets` that have been further calibrated by a jet energy scale (JES). This is a Monte Carlo (MC) based correction that targets the effects that varying detector technologies in η introduce and restores further the energy losses due to the non-compensating and sampling nature of the ATLAS calorimeters.

2.4.6.3. Flavor Tagging

For jet reconstruction, *flavor tagging* is an important method to acquire information about whether a jet was initiated from a b-quark. The b-quark represents a notable exception among quarks, as its hadronization products contain b-quarks, typically B-mesons. These mesons have lifetimes of the order of 10^{-12} s [12], re-

sulting in a measurable displacement of their decay position with respect to the interaction point of the initial state particles of typically a few millimeters. A jet that contains a *secondary vertex* (SV) therefore indicates the creation of a b-quark, and is referred to as a b-jet. Algorithms to identify b-jets are referred to as *b-tagging* algorithms, and a selection of those are described in the following.

Most algorithms for b-tagging rely on the lifetimes of B-mesons, which lead to at least one displaced secondary vertex in an event. Since b-quarks can decay into muons, it is also possible to exploit this decay for b-tagging. However, this short overview is focused on lifetime-based b-tagging algorithms [21]. All algorithms of this type rely on the measurement of the particles' trajectories after their creation (tracks). They therefore require a detector capable of tracking particles.
To b-tag a jet, the algorithms analyze the tracks associated with the jet of interest. There are two common approaches: based on the impact parameter[10] of tracks (e. g. JetProb and IP3D [21]), and based on finding a secondary vertex in a jet (e. g. SV1 and JetFitter [21]).
To achieve a better b-jet efficiency (achieved by impact-parameter-based algorithms) and better light jet (gluon, or u-, d-, or s-quark induced) rejection (achieved by secondary-vertex-based algorithms), algorithms are often combined to deliver a unified b-tagging weight. A common combination is MV1 [21], which combines IP3D, SV1 and JetFitter via a neural network. A version of the MV1 algorithm that is trained to particularly reject c-jets instead of light jets is referred to as MV1c. Its light jet rejection decreases only minorly.
The currently most powerful b-tagging algorithm is MV2 [22], a boosted decision tree (BDT) based algorithm that, like MV1, takes as input variables the outputs of the basic b-tagging algorithms IP3D, SV1 and JetFitter. Compared to MV1, MV2 significantly simplifies the algorithm, as the input variables of the three basic algorithms are used directly.[11] Also for MV2 a version trained to reject c-jets exists:

[10] The transverse impact parameter, d_0, of a track is the distance of closest approach of the track to the primary vertex (PV) in the plane perpendicular to the direction of the colliding particles. Furthermore, the longitudinal impact parameter z_0 is the distance of the mentioned point of closest approach to the PV in longitudinal direction.
[11] The use of intermediate multivariate layers, like the neural network of the JetFitter algorithm, is omitted.

MV2c. For MV2c it is customary to control the fraction of c-jets with respect to light jets in the sample it is trained with, as this has implications on its c-jet and light jet rejection. The fraction is stated in percentage at the end of the trained algorithm, e. g. MV2c20 or MV2c10.

3. Searches for the Higgs Boson Decaying to $b\bar{b}$

On July 4, 2012 CERN announced the discovery of a particle consistent with the Higgs boson, after many experiments had searched for it over the course of some 50 years. Since then, the ATLAS and CMS experiments continued to probe the new found boson's properties. So far, all LHC measurements, including decay width, couplings to particles, spin, and parity are consistent with SM predictions [23–27]. However, these measurements have been mainly performed in the bosonic decay modes of the Higgs boson ($H \to \gamma\gamma$, $H \to ZZ^*$, $H \to WW^*$). In order to further confirm the mass and SM properties of the found Higgs boson, it is necessary to establish an observation of its fermionic decay channels (mainly[1] $H \to b\bar{b}$ and $H \to \tau\tau$). In particular, it remains to be shown that the Higgs field is the source of mass generation for fermions, and whether the Higgs boson's direct coupling to the quark sector is as predicted by the SM. The efforts of the ATLAS and CMS experiments to observe the Higgs boson decay to a τ-lepton pair have recently lead to an evidence in that channel [28, 29]. The searches in the $b\bar{b}$ channel have not yet reached evidence status. This section will highlight the history of those searches as well as their current state, and explain how the VBF production channel can contribute to an observation of H(bb)[2].

[1] Higgs boson branching ratios to other fermions are considerably smaller and thus meaningful searches in these channels cannot be performed with current integrated luminosities of particle collision data.

[2] Short for $H \to b\bar{b}$.

3.1. Higgs Boson Decays to Beauty-Quarks

As mentioned in Sec. 2.2.3, the Higgs boson predominantly decays into a pair of b-quarks. The search in this decay mode is a particularly challenging one. Firstly, the background from QCD multijet production cannot be reduced by applying b-tagging criteria. At the LHC this background occurs about seven orders of magnitude more often than the signal process [30]. This problem arises in all production channels: in ggF and VBF the b-jets are produced alongside other jets (QCD multijet background), in VH the background becomes $Vb\bar{b}$, and in ttH it is $t\bar{t}b\bar{b}$. Ways to deal with this background include estimating it by studying signal depleted control samples in data, and making use of a fine invariant mass resolution for $b\bar{b}$-dijets.
Furthermore, the background where light quark or gluon jets are produced is $\mathcal{O}(100\,\text{nb})$ [31]. To reduce this background, the light jet rejection factor of the used b-tagging algorithm has to be sufficiently high ($\mathcal{O}(100)$), but at the same time the achieved b-jet efficiency has to be kept at a high percentage.
Due to these reasons, the production modes with additional leptonic signatures (VH leptonic, ttH semileptonic/dileptonic) become increasingly viable with respect to the jet-only topologies for an observation of H(bb). In the following, the history (also prior to the Higgs boson observation) and current status of searches for H(bb) in different production modes are presented.

3.1.1. ggF

The ggF production cross section was one of the first Higgs production mechanisms to be discussed [32, 33]. Initiated through gluons, this production mode can only be studied at hadron colliders. In extensive studies of those colliders [34] it was found that the background for ggF production in case of $m_H < 2m_W$ was many orders of magnitude higher than the signal, discouraging searches for hadronic Higgs boson decays in this mode. In the other case, $m_H > 2m_W$, the ggF is not the dominant production mode (instead VBF dominates this regime) and a search was thus considered to be unfavorable, too. However, more recent studies focussing on the LHC introduced QCD corrections that increased the ggF production cross

section significantly [35–37].
At the LHC, ggF production is the main mode for Higgs bosons searched for in their decays to electroweak gauge bosons (and their subsequent decay to leptons in case of the W/Z), where QCD multijets are not the dominant background. A ggF H(bb) search effort has not been conducted so far.

3.1.2. VH

The associated production of the Higgs boson with a Z or W boson is especially viable because of the possibility of using the leptons of $W \to \ell\nu$, $Z \to \ell\ell$, or the MET of $Z \to \nu\nu$ decays for trigger and background reduction purposes [38].
In early studies of Higgsstrahlung [39–41] it was found that the production cross section turned out to be too low to conduct sensitive studies with the center-of-mass energies and luminosities of existing accelerators (e. g. ISR or SPS).[3] The discussion of VH(bb) was revitalized when it became clear that the top quark was very heavy [42], that the Higgs boson mass exceeds the limit placed by LEP, and that b-tagging[4] will be feasible in high-luminosity hadron collider environments (with the Silicon Vertex Detector [45] of CDF). Studies on the feasibility of the VH(bb) search at the Tevatron as well as the anticipated LHC were conducted [38, 46, 47], and resulted in a prospect where a VH(bb) observation should be possible with $100\,\mathrm{fb}^{-1}$ for an intermediate mass Higgs boson with a mass of 120 GeV. These studies, however, were based on underestimated b-tagging algorithm performances (as is known nowadays). At least since LEP II (1996), all LEP experiments were equipped with vertex detectors [48–51] that made b-tagging possible. This resulted in $e^+e^- \to ZH \to Z + b\bar{b}$ being the main search channel for Higgs boson physics at LEP. Combined, the LEP experiments set a lower limit on the Higgs boson mass of 114.4 GeV [52], using ZH(bb) as the most sensitive channel. Searches for VH(bb) were also performed by the Tevatron Collaborations [53, 54], and resulted in the first cross section limits from hadron colliders. The VH(bb)

[3] Note that the number of events used to discover the W and Z bosons at the UA1 and UA2 experiments at the SPS were $\mathcal{O}(1)$. Early cross section predictions for Higgs boson production via Higgsstrahlung were over a hundred times smaller than the cross section for Z or W boson production [40]—even for light Higgs bosons.
[4] Tagging of heavy long-lived particles for Higgs boson detection was first proposed in the early 1980s [43, 44].

searches at the Tevatron ended with an evidence consistent with the production of the Higgs boson in the mass range 120–135 GeV [55].
Nowadays, VH is the LHC's main channel in the H(bb) search, and is the one closest to an evidence: The observed deviation from the background-only hypothesis corresponds to a significance of 1.4 standard deviations at the ATLAS experiment [56]. The dominant backgrounds are $(W/Z)+$jets and $t\bar{t}$ events, as well as multijet events where jets are misidentified as electrons, or where heavy-flavor quarks decay semileptonically. Searches in this decay mode are usually performed in the 0ℓ, 1ℓ, and 2ℓ channels separately, and to improve the significance the channels are split further according to the transverse momentum of the vector boson.[5]
The ATLAS and CMS experiments are actively searching for VH(bb). Using the Run 1 dataset, the CMS collaboration reports an upper limit of the production cross section times branching fraction at the 95 % confidence level of about 1.89 times the SM prediction[6] [57], while the ATLAS analysis reports 1.2 for the same quantity [56].

3.1.3. ttH

The ttH production mode allows for a direct measurement of the Yukawa coupling of the top quark. The ttH channel can thus help exclude proposed extensions of the SM [58] that result in an increased top-Higgs coupling, or help find a non-SM Higgs boson.
Due to the top quarks produced in association with the Higgs boson, and their very distinct decay patterns, a separation of the signal from background events becomes feasible.
The first cross section calculations of this production mode were given by [59, 60],[7] and it was acknowledged that the cross section falls behind that of the ggF pro-

[5] The background composition varies among the different p_T^V categories, and the high p_T^V categories have a better signal-to-noise ratio.
[6] In the following, analogous quantities will be referred to as "upper limit on $\sigma \times$ BR." When no specification of m_H is given, a Higgs boson mass of 125 GeV is implied.
[7] Besides that, the Higgs boson production by heavy-quark flavors, alongside the ttH Feynman diagram, was mentioned in a publication about the ggF mode [33]. However, no cross sections were calculated.

duction. Still before the discovery of the top quark,[8] but after the exclusion of light Higgs bosons [62], the discussions in ttH were mainly targeting the more distinct decay channels involving leptons and photons [61, 63]. With the exclusion of light intermediate mass Higgs bosons [64], more research was done in assessing also the viability of the ttH mode with a decay of the Higgs boson into b-quarks—an observation of ttH(bb) was prospected to become feasible with $\mathcal{O}(100)\,\mathrm{fb}^{-1}$ of pp collision data [65–67]. The first analysis in the ttH(bb) channel was performed within the CDF experiment (Run 2) at Fermilab, where an upper limit on $\sigma \times \mathrm{BR}$ of 176 (for $m_H = 115\,\mathrm{GeV}$) was reported [68]. Later, the DØ collaboration published first results, too, and reported an upper limit on $\sigma \times \mathrm{BR}$ of 84.8 [69].[9]
Both the ATLAS and CMS experiments conducted searches in this production channel in the LHC Run 1; searches that make use of the semileptonic and dileptonic top pair decay channels [72–74], or the hadronic channel [75]. The CMS collaboration reports an upper limit on $\sigma \times \mathrm{BR}$ of about 4.1 [73], and the ATLAS analysis in the semi/dileptonic channels reports 3.4 for the same quantity [72].[10]

3.2. Vector Boson Fusion Higgs Boson

This section gives an overview of the Higgs boson's VBF production mode, which can contribute to enhance the sensitivity in the $b\bar{b}$ decay channel. With the second highest production cross section at the LHC and a distinct event topology the VBF production mode provides beneficial features.

3.2.1. History

The VBF production mode was first considered when studies about the feasibility of Higgs boson searches at e^+e^- colliders were conducted [76]. While having a lower

[8] The $pp \to t\bar{t}HX$ production cross section at the prospected LHC was found to be fairly insensitive to the actual mass of the top quark [61], for $m_t \lesssim 200\,\mathrm{GeV}$ and intermediate mass Higgs bosons.

[9] Subsequent analyses by DØ and CDF performed on their respective full datasets could reduce the upper limit on $\sigma \times \mathrm{BR}$ to 74.3 and 20.5, respectively [70, 71].

[10] The most recent ATLAS ttH(bb) publication [75] combines the results of the hadronic and semi/dileptonic ttH(bb) searches of the ATLAS collaboration. However, no upper limit on $\sigma \times \mathrm{BR}$ is quoted, only a combined signal strength of $\mu = 1.4 \pm 1.0$.

cross section than ZH, it was noted that the VBF channel could produce Higgs bosons of higher masses more efficiently than ZH [76, 77]. At prospected multi-TeV hadron colliders, too, VBF would primarily be considered as a means to produce *heavy* Higgs bosons ($m_H > 2m_W$), since in this mass regime the production mode would start to dominate over ggF[11] and VH [44, 78, 79]. Soon, the possibility of using the VBF topology (see Sec. 3.2.3) as a method to identify heavy Higgs bosons was pointed out [80, 81]. However, these studies targeted the dominant decay channel for heavy Higgs bosons, $H \to WW$ and $H \to ZZ$. When LEP was built it was expected to find the Higgs boson if it was $m_H < 80\,\text{GeV}$, and plans for the LHC would have it target the high mass region $m_H > 130\,\text{GeV}$. Unclear was how the intermediate mass region, where the decay $H \to b\bar{b}$ dominates, should be approached with the LHC. Studies were conducted and showed that a LEP/LHC run in an *ep*-mode, where VBF production dominates for all Higgs boson mass ranges, would provide an effective means observing VBF H(bb) [82].[12] The LEP/LHC, however, has not been realized yet. The first LHC (run in *pp* mode) studies for VBF H(bb) suggested that the channel may play an important role in studying the intermediate mass Higgs boson at the LHC [85–88]. The main difficulties were seen in identifying the rapidity gaps (see Sec. 3.2.3) among pileup events.[13] The years until the LHC launch were mainly used to compute corrections to the VBF production cross section and implement MC calculations [89–91]. With the start of data-taking at the ATLAS and CMS experiments the first results would follow a few years after the other more promising channels were searched for.

[11] The calculation was based on an assumed top mass an order of magnitude lower than it actually turned out to be.

[12] The only other *ep* experiment, HERA, lacked the capabilities of searching for the Higgs [44, 83, 84].

[13] Pileup events are interactions (in case of the LHC, proton-proton) that are recorded in the detector alongside the event of interest. They can occur due to multiple proton-proton interactions per bunch crossing, multiple parton-parton interactions per proton-proton collision, or because detection systems have sensitivity time windows longer than the bunch spacing time.

3.2.2. Current State of the Observation

The VBF channel has the second highest production cross section for Higgs bosons at the LHC. In this channel the distinct topology (detailed in Sec. 3.2.3) provides a handle to reject background events (that consist mostly of irreducible $b\bar{b}jj$ multijet events). Both the ATLAS and CMS experiments have published VBF H(bb) searches [92, 93] using data at 8 TeV center-of-mass energy. The CMS collaboration reports an upper limit on $\sigma \times \mathrm{BR}$ of 5.5, while the ATLAS analysis reports 4.4. These analyses are described in more detail in Sec. 3.2.5.
A problem dominant in this production channel is the low trigger efficiency for signal events. In the past it has been $< 10\,\%$.[14] To enhance the trigger efficiency, a variant of the VBF $H \to b\bar{b}$ channel has been proposed: VBF H(bb)+γ [95], which now has an ongoing analysis in the ATLAS Run 2.[15] This channel benefits from a significantly reduced background due to destructive interference occurring between various processes with central photon emission. However, the cross section of the signal process is suppressed by a factor of α (fine-structure constant). In order to achieve a sensitive search, even higher integrated luminosities than for the inclusive VBF H(bb) search are required.
Another approach to increase the trigger efficiency consists of employing triggers that are specifically geared towards the properties of the VBF H(bb) signal—this approach is elaborated in this thesis and is part of the ATLAS Run 2 search effort for VBF H(bb).

3.2.3. Topological Features

This section gives a description of the special topology that VBF H(bb) events show, which will serve as the basis for the developments presented in Sec. 5.
In the VBF production mode, as already indicated in Sec. 2.2.2, two (typically valence) quarks from the colliding protons scatter off each other via vector boson (W or Z) emission, and these fuse into a Higgs boson (Fig. 2.1).

[14] For comparison, VH(bb) triggers are almost fully efficient [94].
[15] In Run 1, the ATLAS experiment had no search in the VBF H(bb)+γ channel.

Jets The vector bosons are emitted by quarks, since they are the only partons able to do so. After production, the Higgs boson decays into a pair of b-quarks. Based on this process the VBF H(bb) final state features four high p_T jets: two light quark jets, and two b-quark jets. The Higgs boson transverse momentum is of the order of M_W and so is the transverse momentum of both light jets [80]. In the following, the two hadronization products of the light quarks will be referred to as *VBF jets* [80] (abbreviated as the JJ pair).
The b-jets from the decaying Higgs boson tend to be in the more central region of the detector. The VBF jets, on the other hand, are likely to be found in the more forward/backward region of the detector, on opposite sides. The pseudorapidity difference between the VBF jets is therefore relatively high. A typical topology is shown in Fig. 3.1.

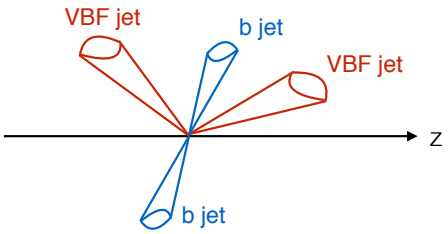

Figure 3.1.: Simplified illustration of a typical topology of a VBF H(bb) event in a detector.

Rapidity Gap The emitted vector bosons are color singlets and thus the emitting quarks do not change color. For this reason, there is no color connection between the initial state quarks, but they interact with their respective proton remnants in order to hadronize, since they are color neutral as a system [96].[16] Additionally, since the Higgs boson is created by an electroweak process, the involved vector bosons are not interacting strongly, and thus are not able to radiate off gluons. As a result, *ideally* the region between the VBF jets is almost free from QCD activity (referred to as *rapidity gap* [97]), except in the region where the Higgs boson decays, since there the b-quarks color connect between each other and

[16] This would change if gluons had been emitted instead of vector bosons. As part of a color octet, the initial state proton becomes colored upon emittance of a gluon and the two initial state hadrons would have to exchange color in order to become color neutral again.

cause hadronic activity. This ideal case can, however, be spoiled by some effects: It was shown in MC studies that even though it is expected that the hadronization products of the remnants of the initial state hadrons stay close to the beam line, many of them still appear in a more central region [96]. Furthermore, pileup events can have an effect on the rapidity gap.
Depending on the chosen model for hadron collisions, the probability that a rapidity gap would "survive" [97] in a VBF event (i. e. that no other parton-parton interaction occurs[17]) was calculated to be between 5.5 % and 22.1 % for an energy around the LHC energy [98].

3.2.4. Background Processes

The dominant background for the VBF H(bb) signal at the LHC are non-resonant multijet events from QCD production, mimicking the signal signature that consists of four high p_T jets. Other backgrounds are hadronic decays of Z (resonant) or W bosons produced in association with other jets, hadronic $t\bar{t}$ decays (i. e. $t\bar{t} \to bW^+\bar{b}W^- \to b + \text{hadrons} + \bar{b} + \text{hadrons}$), and hadronic decays of single top events.

3.2.5. LHC Results

3.2.5.1. Analysis Strategy of CMS

For their recent publication [93] the CMS collaboration employed the analysis strategy of searching for a "signal bump" in the distribution of the $b\bar{b}$ pair invariant mass m_{bb}.
This is done by fitting a combination of MC simulations of background (Z + jets, top pair and single top) and signal (VBF and ggF H(bb)) m_{bb} distributions for different Higgs boson mass hypotheses ("templates" for 115, 120, 125, 130, and 135 GeV) to the data distribution. Additionally, the QCD multijet background is shaped using a data-driven approach. A MC generation of the multijet background is computationally not feasible due to the stringent cuts that are placed for the

[17] Note that this does not account for pileup events of other origins nor for the filling of the gap by the proton remnants.

VBF analysis: far too many multijet events would have to be produced in order to achieve satisfactorily high statistics.
The Higgs boson signal strength is extracted from the m_{bb} distribution in data with a *binned likelihood fit*. The signal strength μ_{H} and the QCD multijet background event yield, N_{QCD}, are free parameters of the histogram likelihood

$$\mathcal{L}(\mu_{\mathrm{H}}, N_{\mathrm{QCD}}) = \prod_{\text{bins b}} \frac{(f_b[\mu_{\mathrm{H}}, N_{\mathrm{QCD}}])^{n_b}\ \mathrm{e}^{-f_b}}{n_b!},$$

where f_b is the value of the fit model $f[\mu_{\mathrm{H}}, N_{\mathrm{QCD}}]$ in bin b of the histogram, and n_b is the observed value (data).[18] It is assumed that n_b follows a Poissonian distribution. Along with the free parameters μ_{H} and N_{QCD}, the fit model f includes parameterized analytic functions for the shapes of the signal and background m_{bb} distributions that have been acquired by fitting analytic functions to the discrete distributions.
In order to enhance the sensitivity, the sample is divided into four categories, and the fit is performed simultaneously for all categories. The categories differ in their signal-to-noise ratio: from mostly background to *signal-enriched*. The latter categories provide high sensitivity, while the background uncertainties are constrained in the former categories, mostly unbiased from signal contribution.
The classification of an event into a specific category is done employing a BDT. For each event, a BDT output variable is computed and based on its value the corresponding category is chosen. The categories are correspondent for a specific range of output values. A BDT is built from input variables chosen in such a way that variables with high separation between signal and background processes and low correlation among each other and with respect to m_{bb} are preferred. The following input variables are considered:

- the kinematics of the VBF jet system: $\Delta\eta_{JJ}$, $\Delta\phi_{JJ}$, and m_{JJ},
- the b-tagging weights of the two best b-tagged jets (highest b-tagging weights),
- the *quark-gluon likelihood (QGL)* for the two best b-tagged jets and the two VBF jets,

[18] The m_{bb} templates are fitted individually; each m_{bb} value has its own $\mathcal{L}$.

- the H_T^{soft} of the event,
- the number N^{soft} of soft trackjets with $p_T > 2\,\text{GeV}$, and
- the angular kinematics of the production: cosine of the angle between the JJ and $b\bar{b}$ planes in the center-of-mass frame of the four leading jets ($\cos\theta^*_{JJ,bb}$).

The variables QGL, H_T^{soft}, and N^{soft} will be explained in the following.

Quark-Gluon Likelihood The VBF topology is characterized by two light quarks that radiate off vector bosons which then fuse into a Higgs boson that subsequently decays. Since the only partons that can radiate vector bosons are quarks, it is useful to require that the VBF jets originated from quarks, and not from gluons, as the same topology could have been formed from gluons radiating off other gluons that fuse and decay into a pair of (b-)quarks (an example of multijet background). To aid the discrimination of these processes on a statistical basis, the quark-gluon likelihood [99] is employed by the CMS analysis.
It has been observed that gluon jets feature a higher charged particle multiplicity, a softer fragmentation function,[19] and are 'wider' (less collimated in the η-ϕ plane) than light quark originated jets [99]. The QGL is a discriminant that is formed by exploiting these differences. For quantification, jets are approximated by an ellipse in the η-ϕ plane whose major and minor axes can be extracted for further processing. The likelihood is computed from the following internal jet composition variables [93]:

- the root-mean square of the distribution of jet constituents along the major axis,
- the root-mean square of the distribution of jet constituents along the minor axis,
- the jet asymmetry pull[20],

[19] So the jet constituents are not so likely to carry a disproportionally large fraction of the total jet energy.

[20] The jet asymmetry pull measures the favored direction in which the internal components of the jet mostly shower towards, relative to the jet center [100]. With respect to the jet center it can be represented in polar coordinates as an angle and a magnitude in the η-ϕ plane. For

- the jet particle multiplicity, and
- the maximum fraction of total jet energy carried by a jet constituent.

From these variables a likelihood-product discriminator is calculated that serves as a measure of probability that a jet originated from a gluon. Fig. 3.2a shows that VBF jets are expected to have low values of QGL, while gluons tend towards a higher QGL.

Soft Hadronic Activity The existence of a rapidity gap between the VBF jets in the VBF topology has been pointed out in Sec. 3.2.3. In order to quantify the QCD activity between the VBF jets, the CMS analysis defines the event variable H_T^{soft}, which is able to statistically distinguish between VBF H(bb) and other processes producing the same final state (ggF H(bb), backgrounds) [93]. The computation of this variable will be explained in the following.
The PV of the event is defined as the reconstructed vertex that ends up with the largest sum of squared transverse momenta of tracks used to reconstruct it. For the PV, a collection of "additional tracks" is built with tracks that

- have $p_T > 300\,\text{MeV}$,
- fulfill *high purity* quality requirements [101],
- are not associated with any of the four leading jets of the event,
- are associated with the PV rather than with other (pileup) vertices, and
- are not in the region between the two best b-tagged jets. This region is defined as an ellipse in the η-ϕ plane with the b-jets as foci, with the major axis having length $\Delta R(b\bar{b}) + 1 = \sqrt{(\Delta\eta_{bb})^2 + (\Delta\phi_{bb})^2} + 1$ and pointing in the direction that connects the two b-jets, and minor axis of length 1.

The selected tracks are subsequently clustered into "soft trackjets" using the anti-k_T algorithm with a distance parameter of 0.5. H_T^{soft} is then computed as the scalar

color flow reasons explained in footnote 16, gluons are expected to tend to pull towards the decay products of the gluon fusion, and not towards the beam line as is the case for VBF quarks.

sum of the p_Ts of soft trackjets with $p_T > 1\,\text{GeV}$. Fig. 3.2b shows the distribution of H_T^{soft} for signal and background events. Due to the rapidity gap, a low H_T^{soft} is expected for signal events, while QCD multijet events statistically have higher values. Lastly, N^{soft} is defined as the number of soft trackjets with $p_T > 2\,\text{GeV}$.

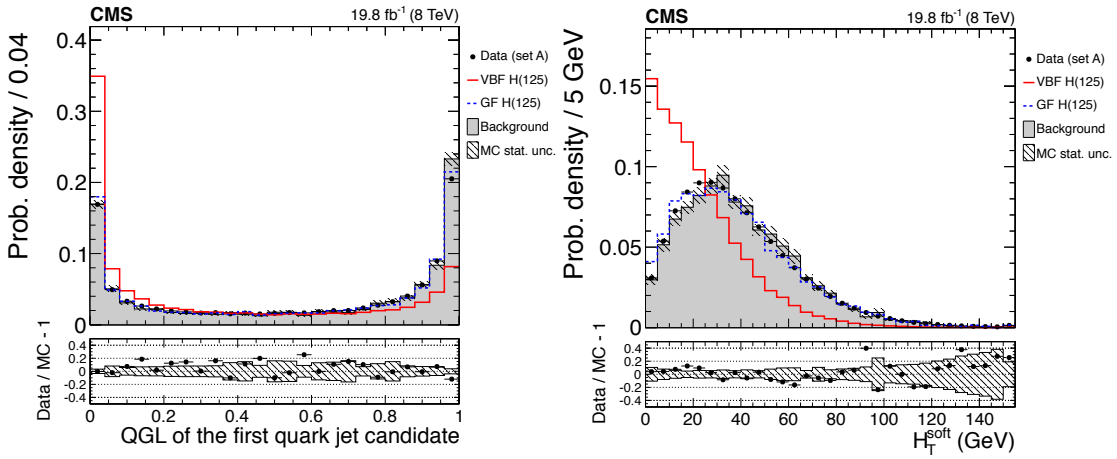

(a) *(b)*

Figure 3.2.: Normalized distributions of (a) the QGL and (b) H_T^{soft} for signal and the sum of all background MC datasets. The bottom panel shows the difference between the data and the background simulation. The shaded band represents the statistical uncertainties in the MC samples. The figures are taken from Ref. [93].

3.2.5.2. Analysis Strategy of ATLAS

The approach used by the ATLAS collaboration in their most recent VBF H(bb) results [92], currently being reviewed for publication, is very similar to the CMS analysis. Here, too, a binned likelihood fit of the different contributing components to the m_{bb} distribution is performed simultaneously in different categories. The categories have been formed by placing different cuts on a discriminant that was built via a BDT. However, there are slight differences in the strategies.

While the CMS analysts only treat μ_H and N_{QCD} as free parameters in the fit, the ATLAS analysis also allows μ_Z (ratio of $Z+\text{jets}$ yield to the SM prediction) to be varied within its theoretical uncertainty around the SM prediction of 1. μ_Z is, as opposed to μ_H, not fitted simultaneously in all categories, but individually in

each of them.
Furthermore, in the ATLAS analysis MC m_{bb} distributions for VBF H(bb) and $Z+$jets are fitted directly to the data histograms (as opposed to fitting an analytic function onto the MC yield which is then in turn fitted with the data). For the non-resonant background both analyses use an empirical parametrized analytical function to fit with the data. However, in the ATLAS search the fit for the dominant QCD background is only performed in the non-signal regions of the data ([70–90] GeV, [150–190] GeV) and is then extrapolated to the signal region.
Compared with the CMS search, the ATLAS search uses different input variables that the BDT is built upon. They are chosen to be discriminating between VBF signal and background events, and to be mostly uncorrelated to m_{bb}, so that the non-resonant background fit in the non-signal regions of the distribution is not influenced by the values of the BDT variables in the signal region. The used variables (ordered by descending discrimination power) are

- the jet widths[21] of VBF jets within $|\eta| < 2.1$ to distinguish quark and gluon initiated jets,
- the scalar sum H_T^{ATL} of p_T of additional (not the VBF or Higgs jets) jets with $p_T > 20\,\mathrm{GeV}$ and $|\eta| < 2.5$,
- the invariant mass m_{JJ} of the two VBF jets,
- the η separation $\Delta\eta_{JJ}$ of the two VBF jets,
- the maximum $|\eta|$ of the two VBF jets,
- the η separation between the average of the VBF jets and the Higgs boson candidate ($\frac{\eta_{J1}+\eta_{J2}}{2} - \frac{\eta_{b1}+\eta_{b2}}{2}$), and
- the cosine of the polar angle θ of the cross product of the VBF jets' momenta in the rest frame of the Higgs boson candidate ($b1$, $b2$ system); this quantity is sensitive to the production mechanism of the event.

[21] The width of a jet is computed by summing up its E_T deposits in the calorimeter, weighted by their angular distance from the jet axis.

4. The ATLAS Experiment at the LHC

4.1. The Large Hadron Collider

The Large Hadron Collider [102] is a proton-proton collider located at CERN (European Organization for Nuclear Research), built within the 27 km circumference tunnel of the previous particle accelerator LEP. Currently, the LHC is the largest of its kind, with a design instantaneous luminosity of $10^{34}\,\mathrm{cm}^{-2}\,\mathrm{s}^{-1}$ and a design center-of-mass energy of 14 TeV—unattained by its predecessors.
The first run of LHC data-taking (Run 1) took place from 2009 to 2013. Within this period, 2011 and 2012 were the years of primary data-taking with *pp* collisions. During these years, the LHC ran with a center-of-mass energy of 7 TeV and 8 TeV, respectively, and an instantaneous luminosity of $\sim 10^{33}\,\mathrm{cm}^{-2}\,\mathrm{s}^{-1}$.
After Run 1 the LHC operations were paused and the machine was prepared for Run 2, which labels the 2015 to 2018 period of data-taking. During Run 2 the center-of-mass energy has been increased to 13 TeV, and the instantaneous luminosity has exceeded its design value. The experiments at the LHC were and continue to be upgraded to cope with the higher luminosity[1] conditions. In 2015, the first $3.2\,\mathrm{fb}^{-1}$ of 13 TeV *pp* collisions were recorded, and data-taking resumed again in 2016, collecting an additional $30\,\mathrm{fb}^{-1}$ as of September 2016.
In the following, the LHC experiment ATLAS is described. A full discussion of its features as well as planned upgrades is beyond the scope of this thesis, which only gives a brief summary of essential information.

[1] Throughout this thesis, a no further specified *luminosity* translates to *instantaneous luminosity*.

4.2. ATLAS

The ATLAS detector [103] is the largest of the experiments housed by the LHC, with a length of 44 m and a height of 25 m, at a weight of approximately 7000 t. It is a hermetic detector and from the interaction point outwards, ATLAS consists of the tracking systems (inner detector), solenoid magnets, calorimeters, toroidal magnets, and muon chamber devices.

4.2.1. Coordinate System

ATLAS uses a right-handed coordinate system with origin in the experiment's nominal interaction point (IP), centered in the detector. The z-axis points along the beam pipe, the x-axis from the IP to the center of the LHC ring, and the y-axis points upwards. In the transverse plane (x-y) cylindrical coordinates (r, ϕ) are used, where r is the transverse distance from the beam pipe, and ϕ the azimuthal angle around the beam pipe. The polar angle θ defines the pseudorapidity η as $\eta = -\ln\tan(\theta/2)$. Distances in the η-ϕ plane are defined as $\Delta R = \sqrt{(\Delta\eta)^2 + (\Delta\phi)^2}$. The transverse energy and momentum are defined as $E_T = \mathrm{E}\,\sin\theta$ and $p_T = \mathrm{p}\,\sin\theta$, respectively.

4.2.2. Tracking System

The tracking detector is required in order to reconstruct the trajectories of charged particles (tracks) created in a collision event. The detector itself is made of silicon (Si) pixels and strips paired with a transition radiation tracker (TRT). The granularity of the tracking system is very high[2] to provide both a sufficient separation power for tracks and a low occupancy. To allow determination of charged particles' momenta and charge, the inner detector is surrounded by superconducting solenoid magnets delivering a 2 T field in direction of the beam axis. The overall tracking system achieves a range coverage[3] of $|\eta| < 2.5$ and a resolution of $\sigma_{p_T}/p_T = 0.05\,\%\; p_T \oplus 1\,\%$, with p_T in GeV.

[2] The highest granularity is achieved by the pixel detector with a minimum pixel size in r-$\phi \times z$ of $50 \times 400\,\mu\mathrm{m}^2$.

[3] Beyond $|\eta| = 2.4$ the tracking performance decreases rapidly. b-tagging is only possible within the coverage of the tracking system.

4.2.3. Calorimeters

The detector's calorimeter system measures the energies of (charged and neutral) particles created at collision events. Within the process of measurement the particles are destroyed. The ATLAS calorimeter system consists of various subsystems: the liquid-argon (LAr) electromagnetic barrel (EMB), the tile barrel, the extended tile barrel, the LAr electromagnetic end-cap (EMEC), the LAr hadronic end-cap (HEC), and the LAr forward calorimeter (FCal). All subdetectors have non-compensating[4], sampling designs, alternating active readout and dense passive layers that collect energy deposits via scintillation or ionization, and induce showers, respectively. The total calorimeter coverage comes to $|\eta| < 4.9$.

4.2.3.1. LAr Electromagnetic Barrel

This part of the ECal extends over $|\eta| < 1.475$. It uses lead as its passive, shower-inducing, material and LAr as the active material. The EMB is separated in three layers longitudinally, the first layer being the most finely segmented subsystem of the ATLAS calorimeters, with a granularity of $\Delta\eta \times \Delta\phi = 0.025/8 \times 0.01$. It provides particularly good capabilities to identify individual photons from π^0 decays.[5] The remaining two layers have coarser resolution.

4.2.3.2. Tile Barrels

Behind the EMB and EMEC, the HCal components tile barrel and extended tile barrel are located. Combined, the pseudorapidity range < 1.7 is covered. Steel is used as the passive material, while the active parts consist of polystyrene scintillating tiles. Like the EMB, it consists of three layers: the two inner layers have the finest granularity ($\Delta\eta \times \Delta\phi = 0.1 \times 0.1$), while the third layer has coarser resolution (0.2×0.1).

[4] *Non-compensating* denotes that energy is lost within the passive layers that is not measured in the active layers. The full energy readout will not equal an incoming particles' energy, but will be lower.

[5] π^0 mesons decay into two (often collimated) photons with a branching ratio of 98.8 % [12].

4.2.3.3. LAr Electromagnetic End-Cap

Each end-cap calorimeter is divided into an outer and an inner wheel that cover the ranges $1.375 < |\eta| < 2.5$ and $2.5 < |\eta| < 3.2$, respectively. Like in the EMB, Pb-LAr is used as the material combination. The outer wheel is separated into three longitudinal layers, while the inner wheel consists of two layers. The granularity for the outer wheel is better than or equal to $\Delta\eta \times \Delta\phi = 0.050 \times 0.1$ for all layers. In the forward region, the inner wheel has a resolution of 0.1×0.1 for both layers.

4.2.3.4. LAr Hadronic End-Cap

The HEC is located behind the EMEC and uses copper and LAr as its material composition. It consists of two independent wheels that are divided into two layers each. The region $1.5 < |\eta| < 2.5$ is covered with a readout cell granularity of $\Delta\eta \times \Delta\phi = 0.1 \times 0.1$, while the range $2.5 < |\eta| < 3.2$ has a lower resolution of 0.2×0.2.

4.2.3.5. LAr Forward Calorimeter

The FCal extends over the range $3.1 < |\eta| < 4.9$ and is divided into three modules: FCal1, FCal2, and FCal3. The first one is designed as an electromagnetic calorimeter and uses copper as its passive material, while FCal2/3 are HCals and use tungsten. All FCal modules use LAr as their active medium. The granularity of the FCal does not easily map to coordinates of $\Delta\eta \times \Delta\phi$ and is therefore usually given in values of $\Delta x \times \Delta y$ [104]. The granularity is relatively coarse, and of the order of centimeters—the coarsest granularity being $\Delta x \times \Delta y = 5.4\,\text{cm} \times 4.7\,\text{cm}$, and the finest being $1.5\,\text{cm} \times 1.3\,\text{cm}$.[6] Approximations for a granularity in values of $\Delta\eta \times \Delta\phi$ are 0.15×0.15 (0.3×0.3) at $|\eta| = 3.5$ (4.5) [105].

4.2.4. Muon Chambers

As muons are too heavy to radiate bremsstrahlung and do not interact strongly, they are not stopped by either the ECal or HCal but are detected in the outermost

[6] For comparison, the second layer of the EMB has a granularity of $\Delta x \times \Delta y = 4.69\,\text{mm} \times 36.8\,\text{mm}$.

layers of the detector, beyond the superconducting toroid magnets[7]—in the muon spectrometer. The additional magnetic field of the toroidal magnets can bend the path of the muons in the z-y plane of the detector, while the solenoid magnetic field only bends in the transverse x-y plane. As a result, the momentum of muons can be determined more precisely by combining the muon chamber track with the track in the inner detector. To acquire the muon tracks, the system uses three layers of monitored drift tubes (covering $|\eta| < 2.7$) and highly granular cathode-strip chambers (covering $2 < |\eta| < 2.7$). Triggering on muons is only possible within $|\eta| < 2.4$ with signals from the resistive plate chambers in the barrel region ($|\eta| < 1.05$) and the gap chambers in the endcap regions ($1.05 < |\eta| < 2.4$).

4.2.5. Trigger and Data Acquisition System

A problem of high luminosity particle colliders is that the rate at which events are produced is too high to store them all. With a bunch spacing time of 25 ns in the LHC Run 2, storing all the 40×10^6 events per second (event rate 40 MHz) would result in over 50×10^6 MB = 50 TB of data per second[8]—mostly containing uninteresting physics phenomena. To decrease the event rate to values that are technically feasible to process and store, and collect only the interesting events, a dedicated trigger and data acquisition (TDAQ) system is used. The trigger system is used with trigger menus, which are tables that determine what events the system is supposed to accept. The menus contain signatures that are likely to be produced by physics processes of interest.

In Run 2, the trigger system consists of two steps of event selection: Level-1 (L1), and High-Level Trigger (HLT). The L1 trigger is based on custom hardware, while the HLT is a software trigger run on commercially available computers.

The L1 trigger searches for *trigger objects*. These include signatures of jets, electrons/photons, high-p_T muons, hadronic τ-leptons, and sums of total and missing transverse energy. For the non-muon signatures it uses all parts of the calorimeter with reduced granularity and precision, and for high-p_T muon detection it uses parts of the muon chambers. The L1 trigger analyzes every event (bunch crossing),

[7] These toroidal magnet give ATLAS its name (A Toroidal LHC ApparatuS).
[8] Average event size of 1.3 MB assumed [103].

but the maximum number of events that can be passed on to the HLT is 100,000 per second (L1 acceptance rate). The HLT has a further reduced acceptance rate of 1 kHz. The L1 and HLT trigger menus have to ensure that the maximum rates are not exceeded.
The HLT uses algorithms that are very similar to offline[9] analysis software, with the constraint of processing time limits. It makes use of the full (non-reduced) granularity and precision of the calorimeter and muon chamber (independently of L1), and also incorporates (limited) tracking information from the inner detector. It is therefore able to trigger on more complex signatures, like secondary vertices from B-hadrons (b-tagging, see. Sec. 2.4.6.3) over the entire event.
Until the end of Run 2 in 2018, wide-ranging changes to the trigger system will have been made [106]. One of them is the addition of a new hardware component to the L1 Trigger: the Topological Processor (L1Topo) [107]. With it, the L1 trigger is capable of making trigger decisions not solely based on simple kinematics of objects, but also by incorporating topological information of the event. These include but are not limited to requirements for angular distributions ($\Delta\eta$, ΔR), invariant masses, or the central transverse energy (HC_T) [108]. The algorithms are, however, limited by processing time and certain constraints apply. For example, invariant mass calculations can only be performed among the leading six jet RoIs (regions of interest; see Sec. 4.2.5.1). Because L1Topo triggers require firmware implementation, changes to the trigger menu cannot be applied on-the-fly.[10]

4.2.5.1. L1 Jets

Due to the restrictions imposed on the L1 trigger by latency requirements, jets at L1 cannot be reconstructed using the methods discussed in Sec. 2.4.6. Instead, "jets" at L1 are simple energy depositions in a coarse η-ϕ grid.
Within the *L1Calo* [109], jets are built from *jet elements*, which in turn are sourced from roughly 7200 trigger towers from all ATLAS calorimeters. The trigger towers are formed by summing the outputs of multiple calorimeter cells (also in depth

[9] The analysis that is performed on permanently stored events (after having been accepted by the trigger system) is referred to as the *offline* analysis. Corresponding to that is the *online* analysis, which is performed in real-time by the trigger system.
[10] Only thresholds can be changed on-the-fly.

between ECal and HCal) and therefore have a reduced granularity.[11] The number of calorimeter cells per trigger tower is dependent on the granularity of the considered calorimeter. Fig. 4.1 shows the granularity of the jet elements that are used to form jets.

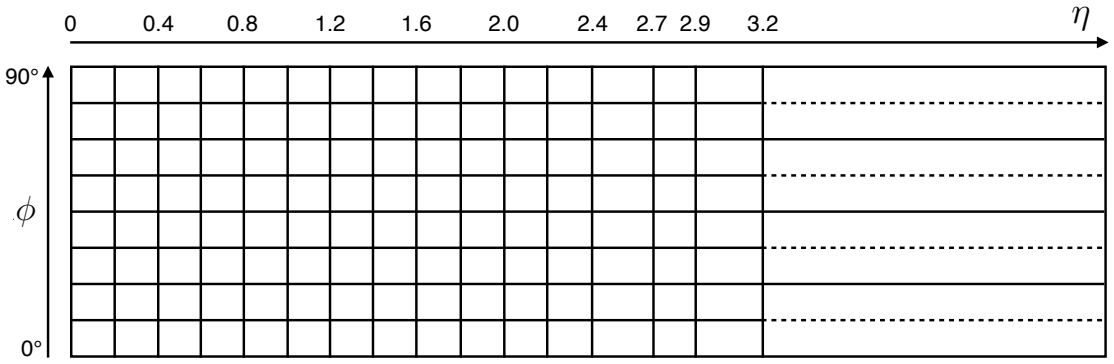

Figure 4.1.: Granularity of jet elements for one quadrant of the detector. In the high precision parts of the detector, the granularity is 0.2×0.2 in $\Delta\eta \times \Delta\phi$. In the forward region the granularity is coarser. The dashed lines in the FCal jet elements indicate that the jet elements are not separated along those lines, but are halved (including their energy) for the purpose of the sliding-window algorithm, so that they appear as simply another pair of jet elements.

On the jet elements a sliding-window jet finding algorithm is run: The sums of E_T in windows of 2×2, 3×3, or 4×4 jet elements (windows of size $\Delta\eta\times\Delta\phi = 0.4\times0.4$, 0.6×0.6, or 0.8×0.8 in the central detector region) are compared against the thresholds of the jet triggers from the L1 trigger menu. Fig. 4.2 illustrates the windows. Within the algorithm, the windows slide in steps of one jet element and overlap. Hence, it is possible that the same jet passes the threshold in multiple windows. In order to prevent these multiple counts, a 2×2 jet elements region (referred to as RoI) within a window is required to be a local maximum, i. e. the RoI is required to exceed the values of all its nearest neighboring 2×2 RoIs (8 total; they do not have to lie within the window). Otherwise, the window is not counted as a jet.

[11] In the region $|\eta| < 2.5$, the trigger towers have a granularity of $\Delta\eta \times \Delta\phi = 0.1 \times 0.1$. Towards more forward regions the granularity becomes coarser.

Finally, the position of the local maximum defines the position of the jet,[12] while its E_T is determined by the sum of the jet elements in the whole window.

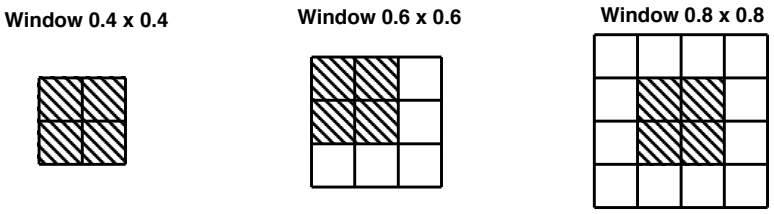

Figure 4.2.: Window sizes of the L1 jet algorithm. $\Delta\eta \times \Delta\phi = 0.2 \times 0.2$ jet elements are combined to jet RoIs (shaded). For the 0.6×0.6 case there are four possible RoIs within the window. The one whose neighbors have the highest E_T sum is chosen as the candidate for a local maximum. In the 0.8×0.8 case, the RoI is required to be in the center. In the forward region the windows have different dimensions in $\Delta\eta \times \Delta\phi$ and are non-squared. The figure is taken from Ref. [103].

4.2.5.2. Prescaling

In order to make efficient use of the allowed bandwidth under various luminosity conditions, trigger menu items (*triggers*) can be prescaled to a number or a fixed rate. If a trigger is prescaled and an event is accepted by that specific trigger it is not given that the event will be passed on for further evaluation or storage. Instead, if the trigger is prescaled to a number, e. g. 20, only every 20th event of that kind is passed on. If the trigger is prescaled to a fixed rate, e. g. 1 Hz, only a maximum of one event per second is passed on. A trigger that has no prescale is referred to as being *unprescaled*.

4.2.5.3. Trigger Naming Convention

Trigger menu items are identified by their name, which also determines the requirements of the trigger. In order to have unambiguous trigger names, a naming convention [110, 111] is employed. Its relevant parts for this thesis (jet triggers) are presented in this section.

[12] The position of the local maximum (position of the RoI) is defined as the geometric center of the RoI, which does not have to lie on the grid lines shown in Fig. 4.1.

Generally, trigger object requirements in trigger names follow the scheme

<N><TYPE><THRESHOLD><RANGE><ADDITIONS>,

where the variables are, from left to right: the multiplicity of the object (omitted if equal to 1); the type of the object (e. g. jet); the threshold applied to the transverse momentum (HLT) or transverse energy (L1) of the object (in GeV); the pseudorapidity range the object is required to satisfy;[13] additional specifications for the object (at HLT level e. g. b-tagging requirements, reconstruction algorithm, calibration, etc.).

Trigger names are composed of the specification of the level (L1 or HLT) followed by an underscore and one or more trigger object requirements (sorted by descending threshold), in turn concatenated with underscores. L1 trigger object requirements are written in capital letters, while HLT ones are lowercased. The L1 seed of an HLT trigger is explicitly specified at its end if the seed is not the default one, or for convenience. The underscore after `L1` is then omitted.

The object type *jet* is denoted by `J` for L1 (4×4 jet elements), and by `j` for HLT. If no pseudorapidity range is specified, it defaults to $|\eta| < 3.1$ for L1, and to $|\eta| < 3.2$ for HLT.[14] At HLT level, or with L1Topo also at L1, the detector region of a trigger object can be specified. The region is denoted as a letter after the threshold: A for $\eta > 0$, and C for $\eta < 0$.

If not further specified for HLT jets, they are reclustered from topoclusters in the full calorimeter scan using the anti-k_T algorithm ($R = 0.4$) with calibrations based on the EM+JES scale. b-tagging requirements are specified by adding `b`<algorithm><tagging efficiency> as a jet property. The property can also be added as `b`<[`loose`, `medium`, `tight`]>. This way, the efficiency with which b-jets are tagged can be adjusted, depending on the instantaneous luminosity.[15] Optionally, the configuration `split` can be added to a b-tagging requirement, in order to

[13] For L1 objects, the $|\eta|$ range to be satisfied is multiplied by 10, while for HLT objects it is multiplied by 100.

[14] In Run 2, the default $|\eta|$ range for L1 jets has become 3.1, as opposed to 3.2 in Run 1 [112].

[15] `bloose` corresponds to an efficiency of 85 %, `bmedium` to 77 %, and `btight` to one of the lower efficiencies 70 %, 60 %, 50 %, or 40 %, depending on the rate of the trigger.

use a special method of finding the PV, introduced in Run 2.
Counting of objects is *inclusive* at L1, while at HLT it is *exclusive*.[16] Using the keyword `AND`, trigger requirements can be declared to be run separately from each other, so that the counting of objects is performed separately.

L1Topo triggers are named in an analogous way [108]. Topological trigger object types include quantities such as `INVM` (highest invariant mass between jet RoIs), or `DETA` (highest pseudorapidity difference between jet RoIs). The input trigger objects that these topological objects are computed with can be specified using hyphens.[17] L1Topo introduces the trigger object `AJ` which is *all objects of type J*. Furthermore, list types such as *all* or *s* (sorted) can follow object types, where appropriate. With `AJ` and list types, objects such as the leading and subleading jets (`AJs2`), or all jets with $E_T > 20\,\text{GeV}$ and $|\eta| < 2$ (`AJ20all.ETA20`) can serve as input for topological objects, or requirements on them can be imposed.

[16] This means for example that the trigger `HLT_2j60_bmv2c2070_split_j55_320eta490_3j45_L12J25.0ETA25_J20.31ETA49_5J15` requires 6 jets at HLT level as well as at L1.
[17] Algorithms that compare input objects (such as `INVM`) take two objects as input, whereas others take only one (such as `HT`).

5. Online Selection of VBF $H \to b\bar{b}$ in the ATLAS Run 2

The LHC Run 2 brings some major changes with respect to Run 1: The center-of-mass energy is increased from $\sqrt{s} = 8\,\text{TeV}$ to $\sqrt{s} = 13\,\text{TeV}$, and the instantaneous luminosity is gradually increased[1] to $2 \times 10^{34}\,\text{cm}^{-2}\,\text{s}^{-1}$. As the luminosity increases, the triggers have to be more selective on signal events. Over the course of this thesis, new triggers were developed that will aid the upcoming VBF H(bb) search in the ATLAS Run 2.

This chapter will progressively introduce the new triggers by first recapping the Run 1 and 2015 trigger menus in Sec. 5.1 and Sec. 5.2. Afterwards, a new trigger concept is presented that solves problems that were identified (Sec. 5.3). New triggers are proposed in Sec. 5.4, and their efficiency is presented in Sec. 5.5. The validation of the triggers in data is performed in Sec. 5.6. Lastly, Sec. 5.7 presents the impact of the new triggers on the sensitivity of the search.

Efficiencies and event rates in this chapter are given for a center-of-mass energy of 13 TeV, while event rates are given for an instantaneous luminosity of $2 \times 10^{34}\,\text{cm}^{-2}\,\text{s}^{-1}$ and are MC estimates from the ATLAS Trigger Menu group, if not specified otherwise.

[1] In Run 1, the peak instantaneous luminosity was $0.77 \times 10^{34}\,\text{cm}^{-2}\,\text{s}^{-1}$.

5.1. Run 1 Triggers

Three unprescaled triggers were employed for the ATLAS Run 1[2] results [92, 113]. The primary trigger `EF_2b35_loose_4j35_a4tchad_4L1J15`[3] is available for the complete data-taking period of 2012 ($20.2\,\text{fb}^{-1}$; 2012 run period A-L). The first trigger stage (L1) of this trigger requires 4 jets with $E_T > 15\,\text{GeV}$ and $|\eta| < 3.2$. At the last trigger stage (EF level) this trigger requires 4 jets with $p_T > 35\,\text{GeV}$ and $|\eta| < 3.2$. Two of these jets are required to pass the loose requirements of the IP3D+SV1 b-tagging algorithm [115].[4]
Furthermore, two additional $1b$ triggers that are largely uncorrelated (due to the use of forward jets) to the mentioned $2b$ trigger were employed: `EF_b35_medium_j35_a4tchad_vbf_3L1J15_FJ15` and `EF_b35_medium_j35_a4tchad_vbf_2L1FJ15`. They are available for an integrated luminosity of $4.43\,\text{fb}^{-1}$ and $4.41\,\text{fb}^{-1}$, respectively (2012 run period H2, I, L). At L1, these triggers require jets with $E_T > 15\,\text{GeV}$: 3 central jets ($|\eta| < 3.2$) and 1 forward ($|\eta| > 3.2$) jet for the one trigger, and 2 forward jets for the other. For both triggers, the EF requires the medium requirements of the IP3D+SV1 b-tagging algorithm to be fulfilled for at least one jet. Also, dedicated VBF topology requirements are needed to pass the trigger.[5]
Combining these three triggers the ATLAS internal note quotes a 5.6 % trigger efficiency for simulated VBF H(bb) events [113].

5.2. 2015 Triggers

The trigger efficiency was one of the main bottlenecks of the Run 1 analysis. Due to the higher luminosity, this issue is even more severe in Run 2. It is therefore of importance to optimize the online requirements so that it is possible to maintain a reasonably high efficiency.

[2] In Run 1 the trigger system consisted of three parts of event selection: Level-1 (L1), Level-2 (L2), and Event Filter (EF). In Run 2 EF and L2 were combined into a unified HLT.
[3] The ATLAS trigger naming convention of Run 1 is different from the one employed in Run 2 and can be found in Ref. [114].
[4] For completeness, the L2 requirements to be met are `L2_2b30_loose_4j30_c4cchad` [116].
[5] At L2, the triggers require `L2_b30_medium_j30_c4cchad_vbf` and `L2_b30_medium_j30_c4cchad_vbf`, respectively.

For the 2015 data-taking, the implemented triggers most suited for a VBF topology are listed in Tab. 5.1. The main inefficiency of these trigger chains is their focus

HLT trigger	L1 seed
`HLT_2j35_btight_2j35`	`L1_3J25.0ETA23`
`HLT_2j55_bmedium_2j55`	`L1_4J20`
`HLT_2j55_bmedium_ht300`	`L1_4J20`
`HLT_2j45_btight_2j45`	`L1_4J20`

Table 5.1.: 2015 ATLAS triggers that are most suited for a VBF H(bb) search. Information from the twikis [117], [118]; some information directly from the ATLAS run query [119] from randomly selected 2015 *pp* runs.

on central jets, whereas the VBF topology typically features one or two forward jets, as shown in Fig. 5.1a. More precisely, the events with three or less central jets, but at the same time one or more forward jets represent 41 % of the events. These events are not selected by the triggers listed in Tab. 5.1. However, an inclusion of the full pseudorapidity range, i. e. `L1_4J20.0ETA49`, was found to have an unsustainable rate at luminosities of $10^{34}\,\mathrm{cm}^{-2}\,\mathrm{s}^{-1}$ and higher.

5.3. 2016 L1 Trigger Concept

The trigger concept that will be introduced in this section exploits the features of the VBF H(bb) topology highlighted in Sec. 3.2.3. Two central jets from the Higgs boson decay and two VBF jets with a rapidity gap are the topology's most prominent features. Fig. 5.1a shows the number of central and forward truth jets with $p_T > 20\,\mathrm{GeV}$ in VBF H(bb) events. Events that have one forward jet mostly have 2 or 3 central jets. Events that contain 2 or more forward jets typically feature 1 or more central jets. And lastly, events without forward jets typically have 3 or 4 central jets. Fig. 5.2 shows schematically the three topologies. Furthermore, the fourth leading jet in VBF H(bb) events typically is of low p_T, as shown in Fig. 5.1b. However, multijet triggers, like `L1_4J20`, require high p_T tresholds at offline level in order to reach their efficiency plateau. Fig. 5.1b shows that these requirements significantly reduce the amount of events available offline.

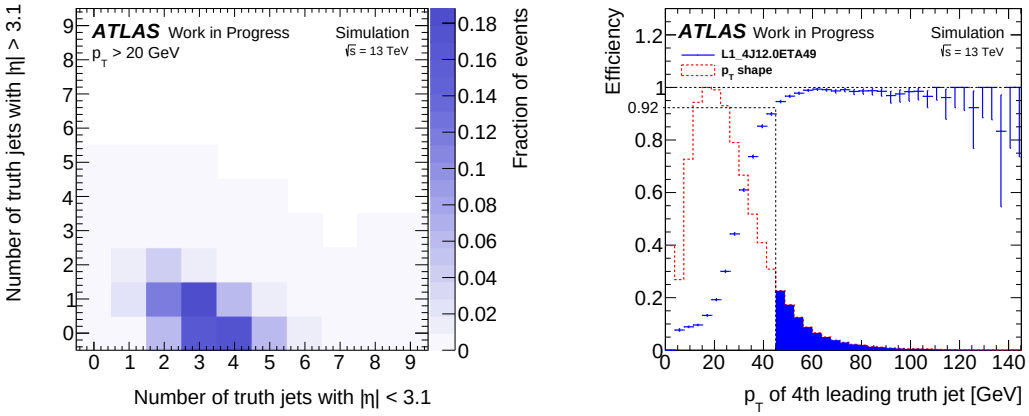

Figure 5.1.: Quantities describing VBF H(bb) events. (a) Number of central and forward truth jets with $p_T > 20\,\text{GeV}$ in VBF H(bb) events. Most events have no or one forward jet and three or four central jets. (b) Efficiency of `L1_4J12.0ETA49` with respect to a selection of four truth jets over the entire η range. $E_T = 12\,\text{GeV}$ is the lowest threshold for L1 jets that can be triggered on. The shaded area is the amount of events that would pass a p_T requirement at the point where the efficiency plateau is reached ($p_T = 45\,\text{GeV}$ with 92 % efficiency). This fraction corresponds to 10.7 % of all events.

An additional study among truth jets with $p_T > 20\,\text{GeV}$ was conducted to assess how often the VBF and b-jets of the topology are found in the respective detector regions. It was found that around 58 % of the events have at least one VBF jet in the forward region, and both b-jets are central; 14 % of the events have both VBF jets in forward regions, and at least 1 b-jet in the central region; while in 20 % of

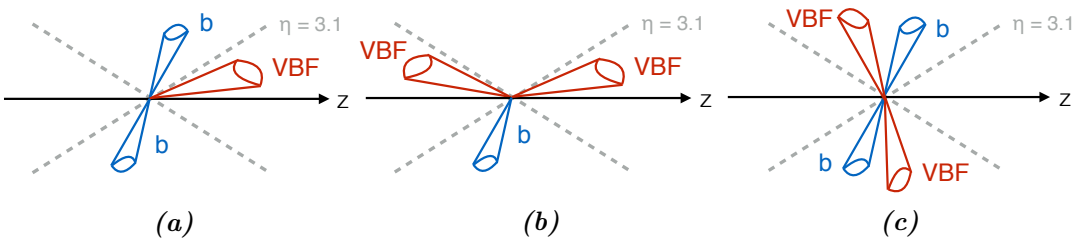

Figure 5.2.: Simplified illustrations of various VBF H(bb) event topologies.

the events both VBF jets and both b-jets are found centrally. These numbers point out that forward jets are an important feature of the VBF H(bb) decay signature.

To target the event topologies of Fig. 5.2 (along with the percentages presented above) while still maintaining a reasonable rate, it would be ideal to employ multiple L1 triggers that each select one of the signatures:

A Targeting the topology of Fig. 5.2a, it is triggered on events with 1 forward jet ($|\eta| > 3.1$) and 2 central jets ($|\eta| < 3.1$). In addition to the case where two of the b-jets are central, this includes cases with a more central VBF jet and where one of the b-jets from the Higgs boson is too soft to be reconstructed as an L1 jet.

B The topology illustrated in Fig. 5.2b requires 2 forward jets that are in opposite sides of the detector (i. e. have pseudorapidities with different signs), and 1 central jet.

C The more central event shape (Fig. 5.2c) is already addressed by `L1_4J20`. However, in order to increase the efficiency, it can also be approached with topological observables. In this case, a minimum HC_T (the scalar sum of the E_Ts of the leading central jets), and a minimum requirement on the maximum $|\Delta\eta|$ between jets in the event are imposed.

The selection for triggers A–C is optimized with the goal of achieving a significantly increased efficiency of triggering on VBF H(bb) events with `L1_4J20` and the new triggers combined, while at the same time keeping the unique rate[6] of the new L1 triggers below $\sim$ 0.5–3 kHz, and of the corresponding HLT triggers below a few Hz.
Trigger C requires the L1 trigger upgrade L1Topo (see Sec. 4.2.5), as does B, since the pseudorapidity is only available in absolute value without the upgrade (rendering the "opposite sides" (OS) requirement impossible to realize). L1Topo is expected to be available in Fall 2016. Meanwhile, ATLAS has resumed to take pp

[6]The unique rate is the additional rate that a respective trigger accepts with, after accounting for the decisions of triggers that are already included in the menu. It is estimated as described in App. A.2.

collision data in May 2016, and will have recorded $\mathcal{O}(10)$ inverse femtobarn until L1Topo is fully implemented.

5.4. 2016 Trigger Implementation

In order to implement the new triggers in the early 2016 data-taking, it was concentrated on optimizing the new triggers A and B (omitting the OS requirement), deferring the optimization of C until L1Topo becomes available.

Without major upgrades of the L1 firmware—which would not have been implemented in time for the beginning of the data-taking—new triggers had to be built by combining existing L1 items:

- Jets ($|\eta| < 3.1$): `J12`, `J15`, `J15.0ETA25`, `J20`, `J25`, `J30`, `J40`, `J50`, `J75`, `J85`, `J100`, `J120`, `J400`,
- VBF topology jets: `J20.0ETA49`, `J30.0ETA49`, `J15.23ETA49`, `J40.0ETA25`, `J20.28ETA31`, `J25.0ETA23`,
- Forward jets ($3.1 < |\eta| < 4.9$): `J15.31ETA49`, `J20.31ETA49`, `J30.31ETA49`, `J50.31ETA49`, `J75.31ETA49`, `J100.31ETA49`.

Tab. 5.2 summarizes the rates and VBF H(bb) efficiencies for the proposed triggers that combine existing L1 items. Furthermore, the proposed HLT parts for the L1 triggers are given. The HLT trigger requirements do not alter the offline selection at which the L1 triggers reach their efficiency plateau (see Sec. 5.5). Along with the proposed triggers, Tab. 5.2 also lists the most relevant 2015 trigger that is also implemented in the 2016 trigger menu: `HLT_2j45_bmv2c2070_split_2j45_L14J20`,[7] which is referred to as the "2015 trigger" in the following.
The new triggers listed in Tab. 5.2 have sufficiently low rates, and were implemented into the 2016 trigger menu for data-taking (unprescaled). The HLT support triggers,

`HLT_j80_0eta240_j60_j45_320eta490` with `A` at L1, and

[7] `HLT_2j45_btight_2j45` in Tab. 5.1. `HLT_2j55_bmedium_2j55` is no longer included in the 2016 trigger menu, and the other triggers listed in Tab. 5.1 are less relevant.

HLT_j80_0eta240_2j60_320eta490 with B at L1,

were implemented as well, each prescaled to a fixed rate of 0.5 Hz. The new triggers began taking data from 2016 run period A4 onwards.

Trigger	VBF H(bb) eff.	Raw rate [Hz]
L1_4J20	8.36 %	1410
L1_J40.0ETA25_2J25_J20.31ETA49 (=: A)	14.6 %	2030
L1_J40.0ETA25_2J15.31ETA49 (=: B)	4.48 %	270
A $\vee$ B	16.7 %	2310
A $\vee$ B $\vee$ L1_4J20	23.7 %	3720
HLT_2j45_bmv2c2070_split_2j45	2.73 %	49.8
HLT_j80_bmv2c2070_split _j60_bmv2c2085_split_j45_320eta490 (=: A_{HLT})	1.43 %	13.5
HLT_j80_bmv2c2085_split_2j60_320eta490 (=: B_{HLT})	0.23 %	0.5
$A_{HLT} \vee B_{HLT}$ (=: AB_{HLT})	1.62 %	14.0
$AB_{HLT} \vee$ HLT_2j45_bmv2c2070_split_2j45	4.21 %	63.8

Table 5.2.: Implementation of the triggers A and B. Trigger C has not yet been optimized, since the upgrade it requires, L1Topo, is not yet available. The HLT triggers require their respective L1 triggers, although not explicitly indicated.

5.5. Offline Efficiency

In this section, the offline efficiencies that can be reached with the 2016 triggers are presented. They are obtained after applying offline "baseline" selections under which the triggers reach their efficiency plateau, determined in the following.

5.5.1. Offline Baseline Selection for the 2015 Trigger

Fig. 5.3 shows the efficiency of the kinematic part of HLT_2j45_bmv2c2070_split_2j45_L14J20 as a function of the 4th leading offline jet p_T within $|\eta| < 3.2$. The efficiency plateau of about 90 % is reached at about 70 GeV. The efficiency does not reach 100 % because of the nature of the L1Calo: "jets" are squared towers of energy deposits with a coarse granularity (see Sec. 4.2.5.1). As a result, e. g.

jets hitting the same cell or nearby cells cannot be distinguished from one another (*multijet inefficiency*).
Based on Fig. 5.3, the following baseline offline selection is applied for `HLT_2j45_bmv2c2070_split_2j45_L14J20`: ≥ 4 jets with $p_T > 70$ GeV and $|\eta| < 3.2$, of which 2 are b-tagged at 70 % efficiency.

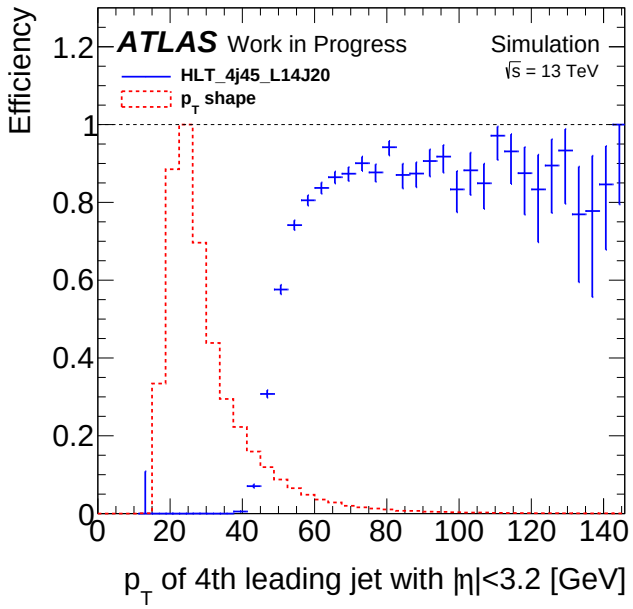

Figure 5.3.: Efficiency for the kinematic part of the 2015 trigger, `HLT_2j45_bmv2c2070_split_2j45_L14J20`, as a function of the 4th offline jet p_T within $|\eta| < 3.2$. Additionally, the shape of the p_T distribution of the 4th leading offline jet is shown. This shape can help estimating how efficient a chosen cut will be.

5.5.2. Offline Baseline Selection for the New 2016 Triggers

The central and forward parts of triggers A and B are independent of each other. The offline selections can therefore be determined individually for the forward and central requirements. In case of trigger A, the two central parts are not independent of each other and are approached in their correct inclusive order (higher thresholds and lower η ranges first).
Fig. 5.4 and 5.5 show the efficiency for the kinematic parts of triggers A and

B as functions of the respective offline jet p_Ts. Derived from these figures, the offline requirements at which the triggers reach their efficiency plateau are shown in Tab. 5.3. Also shown is the achieved value of plateau trigger efficiency. While the 2015 trigger's HLT requirements were already existing, the HLT requirements for the triggers `A` and `B` were newly defined, under the premise that the offline selections under which the L1 triggers reach their efficiency plateau are not altered (see Fig. 5.4 and 5.5).
In addition to the offline requirements listed in Tab. 5.3, b-tagging requirements are applied to the corresponding offline jets that match the HLT b-jet efficiencies. Furthermore, $|\eta|$ requirements are imposed that match the support triggers.

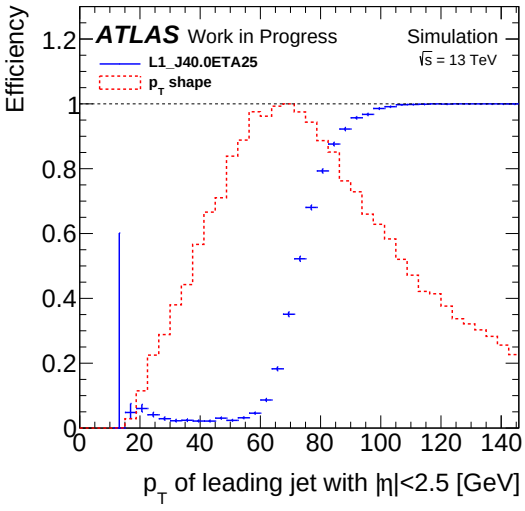

(a) Central part of `A` and `B`: `J40.0ETA25`.

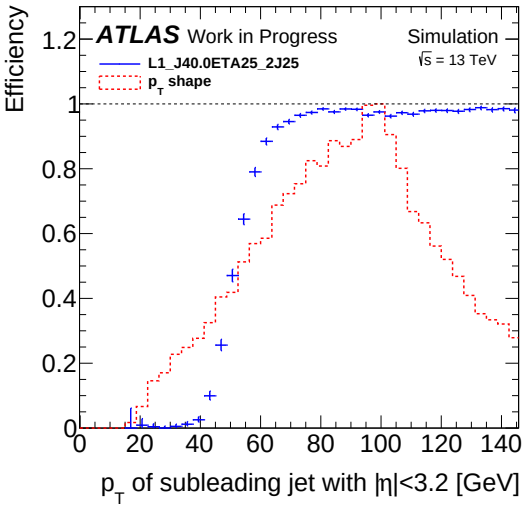

(b) Second central part of `A`: `2J25`, dependent on `J40.0ETA25`.

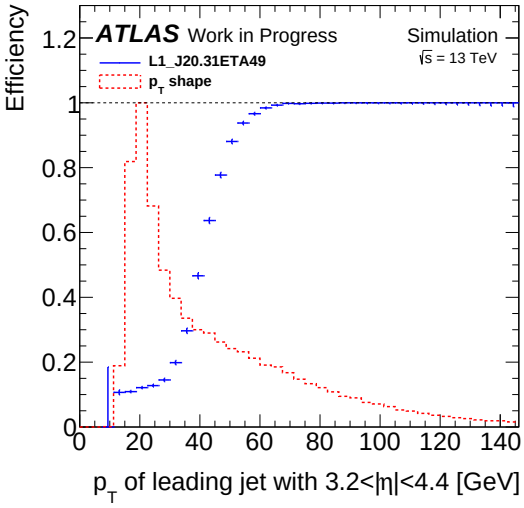

(c) Forward part of `A`: `J20.31ETA49`.

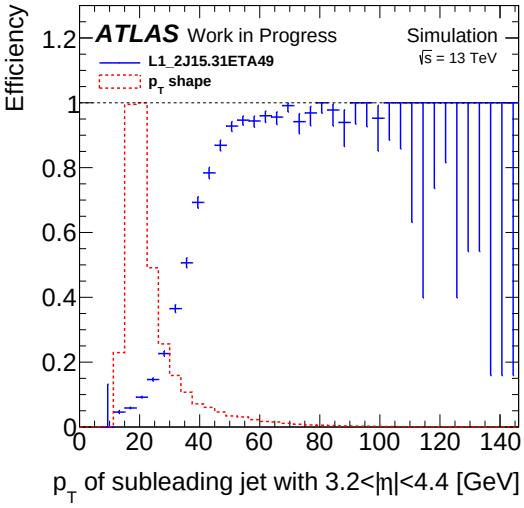

(d) Forward part of `B`: `2J15.31ETA49`.

Figure 5.4.: Efficiencies of the parts of `A` and `B` as functions of the respective offline jet p_Ts. Since the two central parts of `A` are not independent of each other (`J40.0ETA25` and `2J25`), both parts are required in (b). The forward and central parts of `A`, however, are independent of each other, and hence the forward part is approached independently in (c). This independency applies to the forward and central parts of `B` as well. The central part of `B` is the same as for `A` (`J40.0ETA25`), therefore its corresponding offline requirement is adopted from (a). Furthermore shown is the shape of the p_T distribution of the respective offline jet on the x-axis. This shape can help estimating how efficient a chosen cut will be.

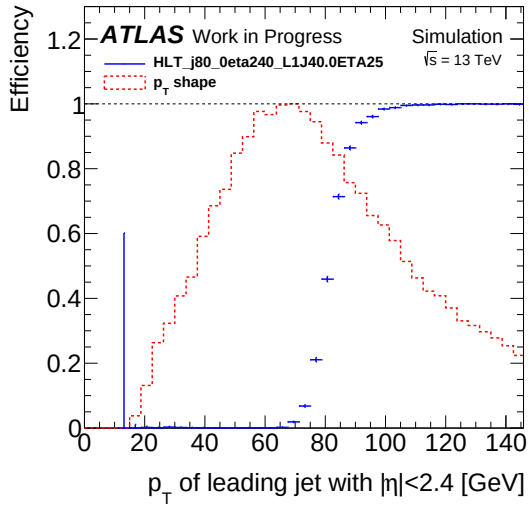

(a) Kinematic central part of $\mathtt{A}_{\mathrm{HLT}}$ and $\mathtt{B}_{\mathrm{HLT}}$: `j80_0eta240`.

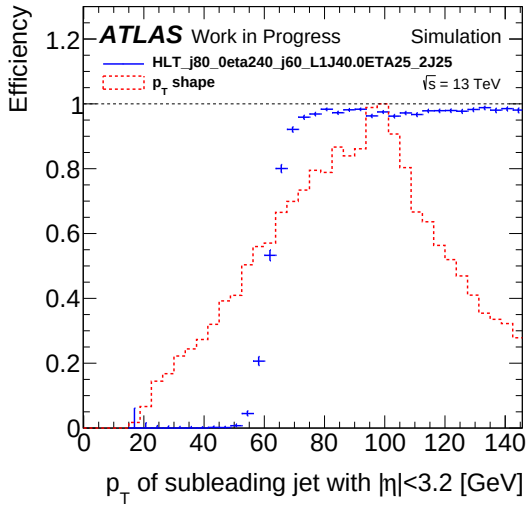

(b) Kinematic second central part of $\mathtt{A}_{\mathrm{HLT}}$: `j60`, dependent on `j80_0eta240`.

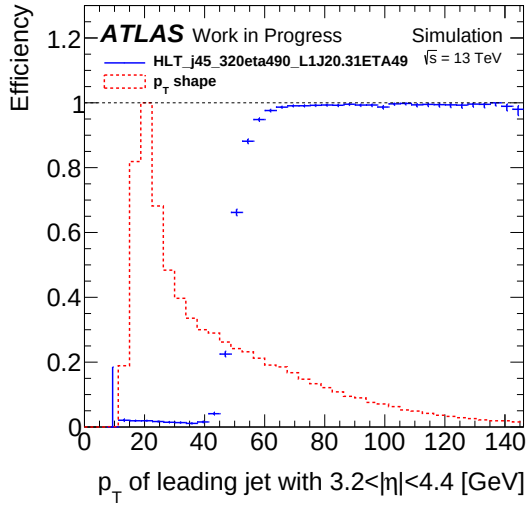

(c) Kinematic forward part of $\mathtt{A}_{\mathrm{HLT}}$: `j45_320eta490`.

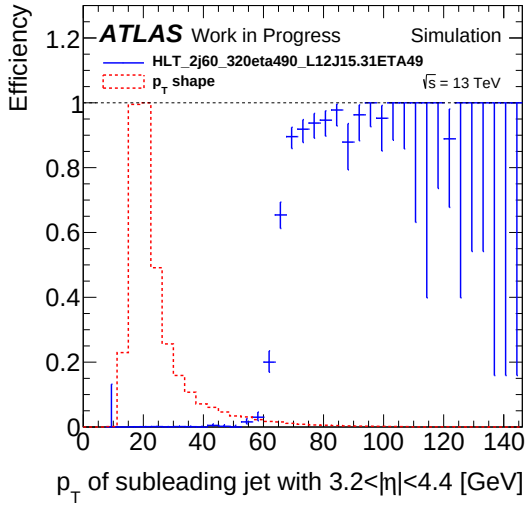

(d) Kinematic forward part of $\mathtt{B}_{\mathrm{HLT}}$: `2j60_320eta440`.

Figure 5.5.: Efficiencies of the kinematic parts of $\mathtt{A}_{\mathrm{HLT}}$ and $\mathtt{B}_{\mathrm{HLT}}$ as functions of the respective offline jet p_Ts. The first central part of trigger $\mathtt{A}_{\mathrm{HLT}}$ is the same as for trigger $\mathtt{B}_{\mathrm{HLT}}$ (`j80_0eta240`), and the offline requirement is determined from (a). The two central requirements of $\mathtt{A}_{\mathrm{HLT}}$ (`j80_0eta240` and `j60`) are not independent of each other, and are therefore both required in (b). However, the forward and central parts of $\mathtt{A}_{\mathrm{HLT}}$ and $\mathtt{B}_{\mathrm{HLT}}$, respectively, are independent of each other, hence the efficiencies are produced independently from each other. Furthermore shown is the shape of the p_T distribution of the respective offline jet on the x-axis. This shape can help estimating how efficient a chosen cut will be.

Trigger	Trigger parts	Offline selection	Trigger efficiency wrt offline selection
2015 trigger	`L1_4J20`, `HLT_4j45`	4 jets with $p_T > 70\,\text{GeV}$ and $\lvert\eta\rvert < 3.2$	$\geq 90\,\%$
A	`L1_J40.0ETA25`, `HLT_j80_0eta240`	1 jet with $p_T > 95\,\text{GeV}$ and $\lvert\eta\rvert < 2.4$	$\geq 96\,\%$
	`L1_J40.0ETA25_2J25`, `HLT_j80_0eta240_j60`	1 jet with $p_T > 95\,\text{GeV}$ and $\lvert\eta\rvert < 2.4$ 2 jets with $p_T > 70\,\text{GeV}$ and $\lvert\eta\rvert < 3.2$	$\geq 95\,\%$
	`L1_J20.31ETA49`, `HLT_j45_320eta490`	1 jet with $p_T > 60\,\text{GeV}$ and $3.2 < \lvert\eta\rvert < 4.4$	$\geq 97\,\%$
B	`L1_J40.0ETA25`, `HLT_j80_0eta240`	1 jet with $p_T > 95\,\text{GeV}$ and $\lvert\eta\rvert < 2.4$	$\geq 96\,\%$
	`L1_2J15.31ETA49`, `HLT_2j60_320eta490`	2 jets with $p_T > 75\,\text{GeV}$ and $3.2 < \lvert\eta\rvert < 4.4$	$\geq 94\,\%$

Table 5.3.: Baseline offline jet selections for the triggers implemented in the 2016 menu. Under these selections the triggers reach their plateau of efficiency with respect to the offline selection.

5.5.3. Overall Efficiency

The offline selections with respect to which the discussed triggers reach their efficiency plateau have been determined in Sec. 5.5.1 and 5.5.2. To proceed, two additional selections are applied:
Selection 1:

- at least 4 jets with $p_T > 20\,\text{GeV}$ and $|\eta| < 4.4$,
- at least 2 b-jets tagged at 70 % efficiency, and
- $p_T^{\text{Higgs}} > 120\,\text{GeV}$.

Selection 2:

- at least 4 jets with $p_T > 50\,\text{GeV}$ and $|\eta| < 4.4$,
- absolute value of the η difference of the VBF jets $|\Delta\eta_{JJ}| > 3$, and
- invariant mass of the VBF jet system $m_{JJ} > 650\,\text{GeV}$.

The Higgs boson candidate is reconstructed from the two best b-tagged jets with $p_T > 20\,\text{GeV}$, and the VBF jets are assigned among the remaining jets above $p_T > 20\,\text{GeV}$ as the pair with the highest invariant mass.
Selection 1 and 2 are applied to all trigger chains and offline baseline selections. Tab. 5.4 compares the efficiencies of triggers A and B, and Tab. 5.5 shows the efficiency achieved with the 2015 trigger as well as the overall combined efficiency.[8] Interestingly, the trigger efficiency for the 2015 menu trigger `HLT_2j45_bmv2c2070_split_2j45_L14J20` is higher than the corresponding value for the new triggers. However, this increased trigger efficiency is not passed on to the offline selection, as the offline efficiency after selection 2 is roughly the same as with the new triggers (compare Tab. 5.4c and 5.5a). The final expected overall efficiency gain from the new triggers is about 90 %.

[8] For the results in Tab. 5.4 and 5.5 the MV2c20 b-tagging algorithm is used.

A cutflow	Eff.
`L1_J40.0ETA25_2J25_J20.31ETA49`	14.6 %
`HLT_j80_bmv2c2070_split_j60_bmv2c2085_split_j45_320eta490`	1.43 %
Offline baseline: 1 jet $p_T > 95\,\text{GeV}$, $\lvert\eta\rvert < 2.4$, b-tagged at 70 % efficiency 2 jets $p_T > 70\,\text{GeV}$, $\lvert\eta\rvert < 3.2$, b-tagged at 85 % efficiency 1 jet $p_T > 60\,\text{GeV}$, $3.2 < \lvert\eta\rvert < 4.4$	0.61 %
Offline selection 1: 4 jets $p_T > 20\,\text{GeV}$, $\lvert\eta\rvert < 4.4$ 2 jets $p_T > 20\,\text{GeV}$, b-tagged at 70 % efficiency $p_T^{\text{Higgs}} > 120\,\text{GeV}$	0.42 %
Offline selection 2: 4 jets $p_T > 50\,\text{GeV}$, $\lvert\eta\rvert < 4.4$ $\lvert\Delta\eta_{JJ}\rvert > 3$ $m_{JJ} > 650\,\text{GeV}$	0.26 %

(a)

B cutflow	Eff.
`L1_J40.0ETA25_2J15.31ETA49`	4.48 %
`HLT_j80_bmv2c2085_split_2j60_320eta490`	0.23 %
Offline baseline: 1 jet $p_T > 95\,\text{GeV}$, $\lvert\eta\rvert < 2.4$, b-tagged at 85 % efficiency 2 jets $p_T > 75\,\text{GeV}$, $3.2 < \lvert\eta\rvert < 4.4$	0.09 %
Offline selection 1: 4 jets $p_T > 20\,\text{GeV}$, $\lvert\eta\rvert < 4.4$ 2 jets $p_T > 20\,\text{GeV}$, b-tagged at 70 % efficiency $p_T^{\text{Higgs}} > 120\,\text{GeV}$	0.04 %
Offline selection 2: 4 jets $p_T > 50\,\text{GeV}$, $\lvert\eta\rvert < 4.4$ $\lvert\Delta\eta_{JJ}\rvert > 3$ $m_{JJ} > 650\,\text{GeV}$	0.03 %

(b)

`OR` eff.
16.7 %
1.62 %
0.69 %
0.44 %
0.28 %

(c)

Table 5.4.: (a), (b) Overview of VBF H(bb) efficiencies acquired with the triggers A and B.
(c) Efficiency of (a) and (b) combined.

2015 trigger cutflow	Eff.
`L1_4J20`	8.36 %
`HLT_2j45_bmv2c2070_split_2j45`	2.73 %
Offline baseline: 4 jets $p_T > 70\,\text{GeV}$, $\lvert\eta\rvert < 3.2$ 2 of them b-tagged at 70 % efficiency	0.61 %
Offline selection 1: 4 jets $p_T > 20\,\text{GeV}$, $\lvert\eta\rvert < 4.4$ 2 jets $p_T > 20\,\text{GeV}$, b-tagged at 70 % eff. $p_T^{\text{Higgs}} > 120\,\text{GeV}$	0.57 %
Offline selection 2: 4 jets $p_T > 50\,\text{GeV}$, $\lvert\eta\rvert < 4.4$ $\lvert\Delta\eta_{JJ}\rvert > 3$ $m_{JJ} > 650\,\text{GeV}$	0.30 %
(a)	

Combined eff. with A and B cutflows
23.7 %
4.21 %
1.27 %
0.98 %
0.58 %
(b)

Table 5.5.: (a) VBF H(bb) efficiencies for the 2015 trigger. (b) Overall efficiency combining the selection chains of A, B, and 2015 trigger.

5.6. Validation

The agreement of simulation and data in terms of trigger efficiencies with respect to the offline selection is validated in $2.6\,\text{fb}^{-1}$ of data recorded in 2016.
In order to counter the event bias that is inevitably introduced by employing a trigger system, a reference trigger is needed. The efficiency curves are then determined only with the subset of the recorded data that passed the reference trigger. The reference is chosen in such a way that the original topology of the triggers of interest is left mostly unaffected. `HLT_g25_loose_L1EM15` is used for this study, since the reconstruction of a photon does not alter the topology largely (assuming the reconstructed photons are mostly misidentified jets).
Fig. 5.6d shows the validation efficiency curve of the kinematic part of `HLT_2j45_bmv2c2070_split_2j45_L14J20` with respect to an offline selection of 4 central jets. The bias that is introduced by the reference trigger is depicted (compare blue and red curves). Also shown in Fig. 5.6 are the efficiency curves for

HLT_4j45_L14J15, a low luminosity version of HLT_4j45_L14J20 that is used in 2016. When the luminosity will have reached $2 \times 10^{34}\,\mathrm{cm}^{-2}\,\mathrm{s}^{-1}$, the low luminosity version HLT_2j45_bmv2c2070_split_2j45_L14J15 and its support trigger are expected to have been replaced by their L1_4J20-based versions.
Fig. 5.7 and Fig. 5.8 show the validation efficiency curves of the triggers A and B with respect to corresponding offline selections.
To achieve a higher efficiency plateau, the η range is reduced at offline level for the second central part of A, and for the triggers requiring 4 central jets, with respect to the selection presented in Sec. 5.5.
The validation efficiency curves introduce minor changes to the offline jet requirements determined in Sec. 5.5 in order to have the triggers reach their efficiency plateau and have MC and data agree with each other: The p_T requirement of the second central jet of trigger A is lowered from 70 GeV to 65 GeV; furthermore, the p_T requirement of HLT_4j45_L14J20 is lowered to 65 GeV, and to 55 GeV for the low luminosity version based on L1_4J15, achieving a $\geq 95\,\%$ efficiency. For trigger B, an OS requirement is introduced for the leading and subleading forward jets at offline level. This allows to lower the p_T requirement[9] of the jets from 75 GeV to 70 GeV.
In contrast to Fig. 5.3, 5.4 and 5.5, the curves in Fig. 5.6, 5.7 and 5.8 start at an efficiency significantly higher than zero. This is due to the use of pileup suppression techniques[10] in Fig. 5.6, 5.7 and 5.8 at offline level, but not at trigger level. With the use of offline pileup suppression techniques, pileup jets are removed at offline level, but still trigger the L1 and HLT chains. This causes a raise of the curve at low p_T, since almost every event has multiple (also non-pileup) low p_T jets which fulfill the offline requirements, while the trigger (requiring high p_T jets) is passed by pileup jets.

[9] This threshold could be set even lower (to 55 GeV) if trigger B had an sides requirement already at HLT level (see Sec. 5.8.2).
[10] Based on tracking information [120].

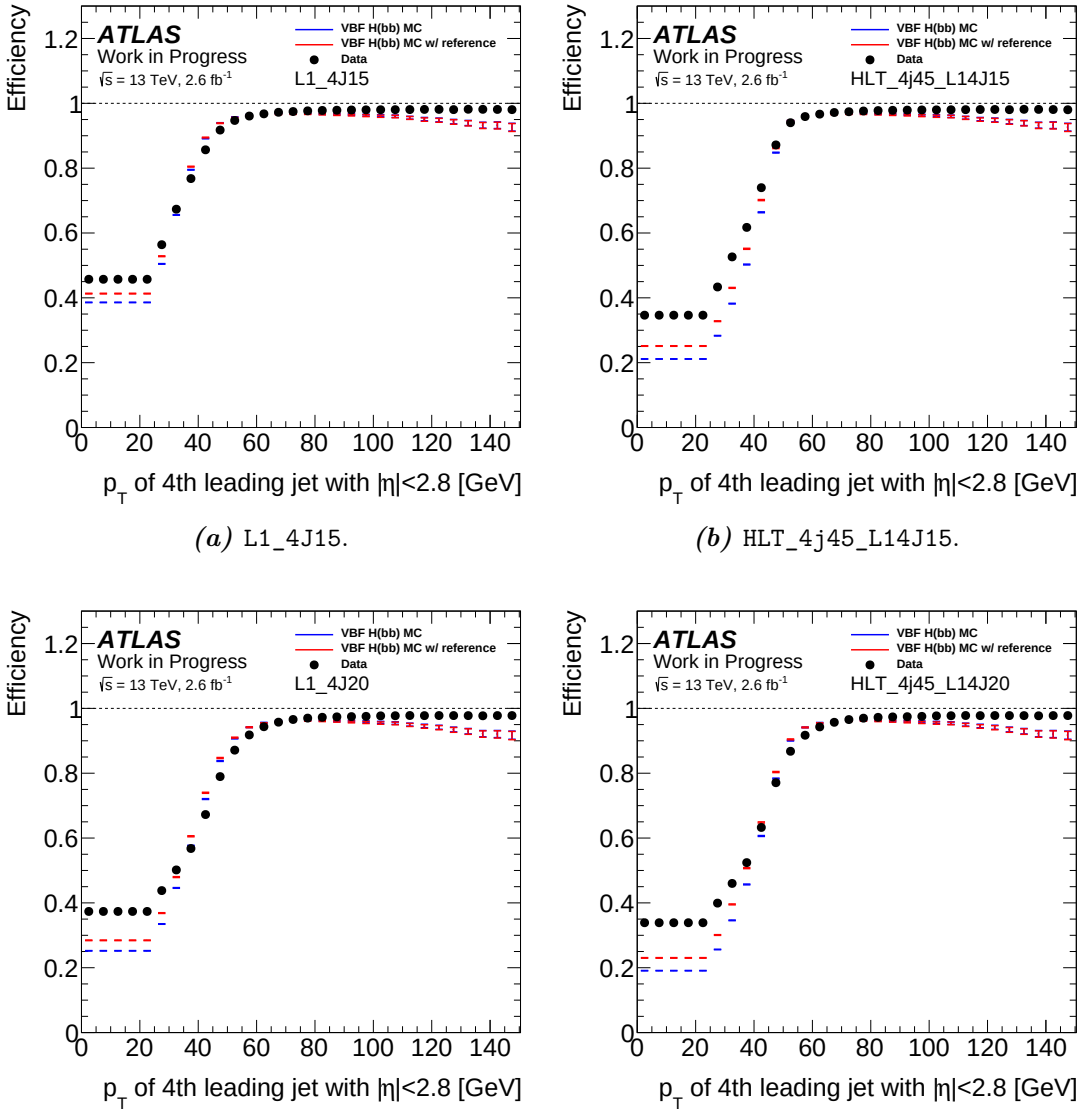

(a) `L1_4J15`.

(b) `HLT_4j45_L14J15`.

(c) `L1_4J20`.

(d) `HLT_4j45_L14J20`.

Figure 5.6.: Validation efficiency curves for the L1 and kinematic HLT parts of the 2015 trigger. The curves are functions of offline jet requirements. The trigger `HLT_g25_loose_L1EM15` is used as reference. Unlike Fig. 5.3, these curves start at an efficiency > 0, since here pileup suppression techniques are applied to the offline jets, but not to HLT and L1 jets.

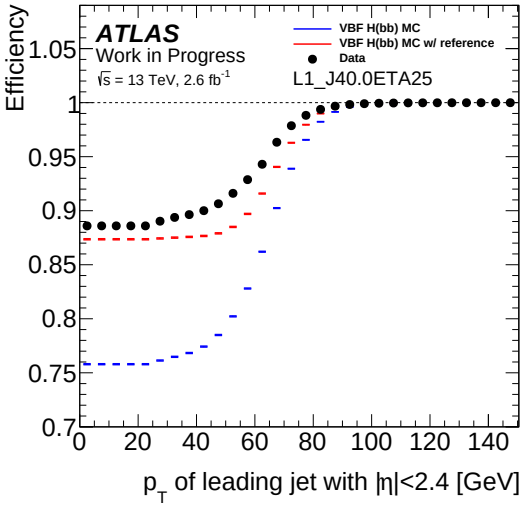

(a) Central part of `A` and `B`: `J40.0ETA25`.

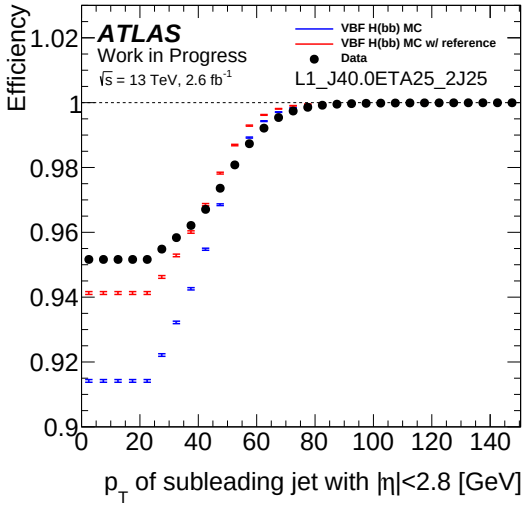

(b) Second central part of `A`: `2J25`, dependent on `J40.0ETA25`.

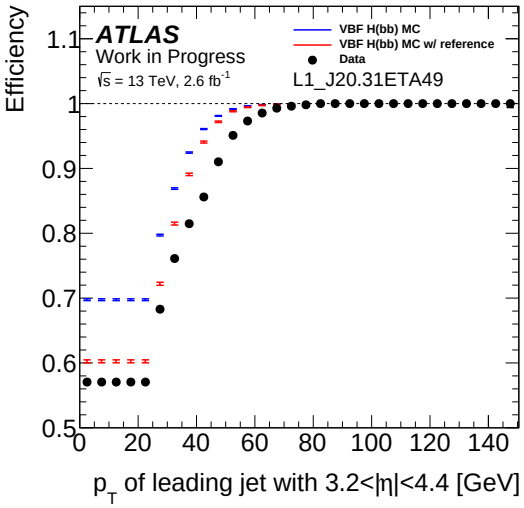

(c) Forward part of `A`: `J20.31ETA49`.

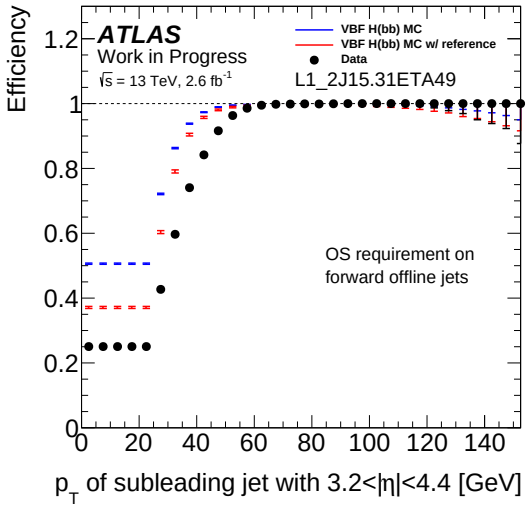

(d) Forward part of `B`: `2J15.31ETA49`.

Figure 5.7.: Validation efficiency curves for `A` and `B`. The curves are functions of offline jet requirements. The trigger `HLT_g25_loose_L1EM15` is used as reference. Unlike Fig. 5.4, these curves start at an efficiency > 0, since here pileup suppression techniques are applied to offline jets, but not to the L1 jets.

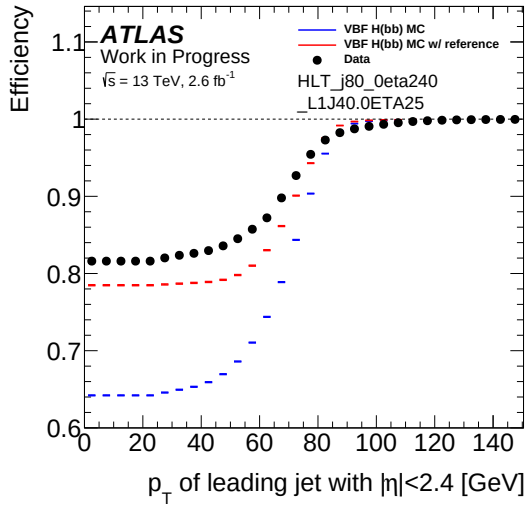

(a) Kinematic central part of A_{HLT} and B_{HLT}: `j80_0eta240`.

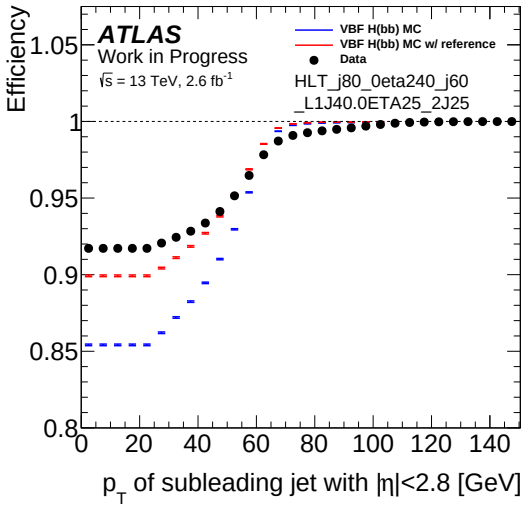

(b) Kinematic second central part of A_{HLT}: `j60`, dependent on `j80_0eta240`.

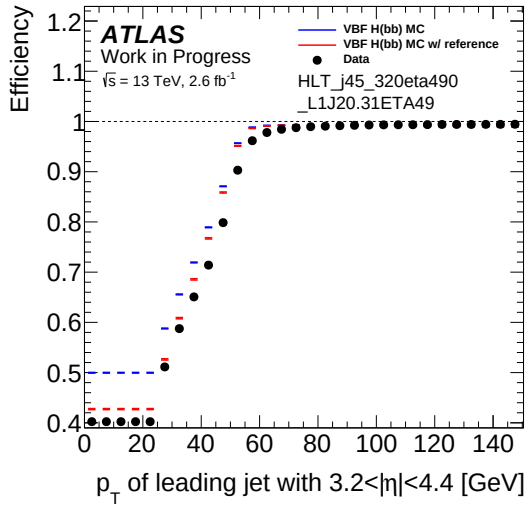

(c) Kinematic forward part of A_{HLT}: `j45_320eta490`.

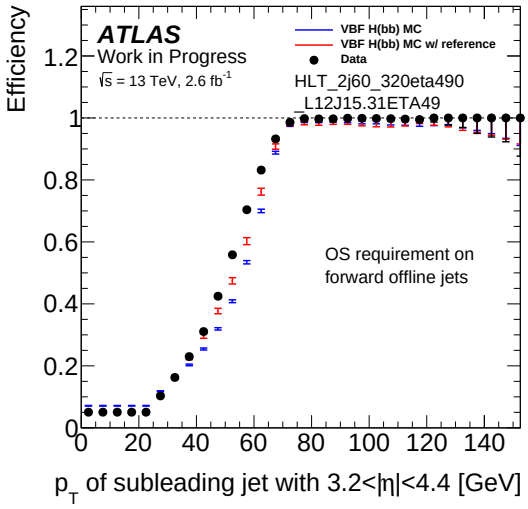

(d) Kinematic forward part of B_{HLT}: `2j60_320eta440`.

Figure 5.8.: Validation efficiency curves for the kinematic parts of A_{HLT} and B_{HLT}. The curves are functions of offline jet requirements. The trigger `HLT_g25_loose_L1EM15` is used as reference. Unlike Fig. 5.5, these curves start at an efficiency > 0, since here pileup suppression techniques are applied to offline jets, but not to HLT and L1 jets.

5.7. Sensitivity Improvement

The impact of the newly implemented triggers on the sensitivity of the VBF H(bb) search is studied in $9.99\,\text{fb}^{-1}$ of 2016 data and is presented in this section.
It was decided to perform this study with the kinematic parts of the triggers (the support triggers), applying b-tagging requirements only at offline level.[11] Since the support triggers are prescaled, determined absolute values of the sensitivity of a trigger are not meaningful, and thus only relative numbers are given.

The sensitivity of a trigger is determined by comparing the number of signal and background events as follows. S is defined as the number of signal events passing the respective trigger, its baseline offline selection, and selection 1 from Sec. 5.5.3, while at the same time fulfilling $100\,\text{GeV} < m_{bb} < 140\,\text{GeV}$. This quantity is computed with MC simulation. The number of events that pass the same selection in data in a certain m_{bb} range is referred to as B. In order not to be biased by signal events, B is calculated from data events of non-signal regions. For this, the requirement on the m_{bb} distribution that it falls linearly in the region $80\,\text{GeV} < m_{bb} < 160\,\text{GeV}$ is imposed. Under this requirement, B is estimated as the sum of the data events recorded in the region $80\,\text{GeV} < m_{bb} < 100\,\text{GeV}$ and $140\,\text{GeV} < m_{bb} < 160\,\text{GeV}$, divided by 2 (computing the average in this region). Finally, the quantity $S/\sqrt{B}$ is referred to as the sensitivity of the trigger.

Fig. 5.9a exemplarily shows for trigger A that the m_{bb} distribution is not linearly falling without the $p_T^{\text{Higgs}} > 120\,\text{GeV}$ requirement. Instead, the p_T cuts combined with the b-tagging requirements favor invariant masses higher than the Z peak, which is dominant without these requirements. Due to this, $p_T^{\text{Higgs}} > 120\,\text{GeV}$ was imposed on the events, as listed in Sec. 5.5.3. This requirement changes the distribution in such a way that the linearity assumption is justified, see Fig. 5.9b.

In order to further improve the sensitivity, requirements on $|\Delta\eta_{JJ}|$ and m_{JJ} are introduced. These are independent of requirements that are imposed on quantities involving the $b\bar{b}$-pair, such as p_T^{Higgs}, or m_{bb}. For each trigger the optimal cut values

[11] This is expected to have little impact on the outcome of the study, since under the offline baseline selections applied, the triggers reach their efficiency plateau.

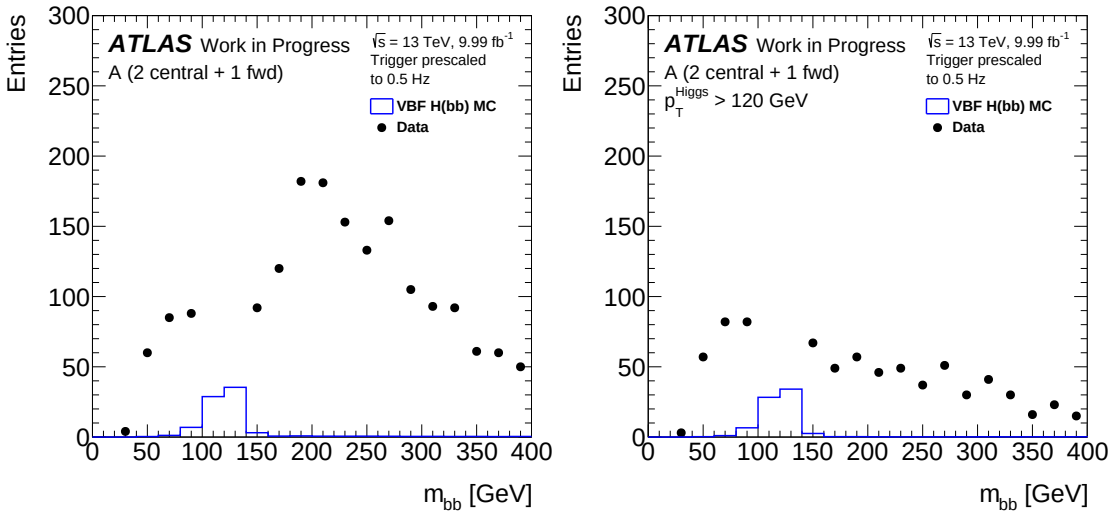

Figure 5.9.: m_{bb} distribution of trigger A (a) without and (b) with $p_T^{\text{Higgs}} > 120\,\text{GeV}$ requirement imposed. The signal region is blinded in data. The event counts in data are based on the trigger decision of the support trigger, which is prescaled. Lower event counts are thus expected with respect to the unprescaled main trigger. The requirement $p_T^{\text{Higgs}} > 120\,\text{GeV}$ has been introduced to approximate the assumption of a linearly falling background distribution.

are found by maximizing $S/\sqrt{B}$, computed from the m_{bb} distribution. Within the optimization, combinations of $|\Delta\eta_{JJ}|$ and m_{JJ} requirements are run through on a fine $|\Delta\eta_{JJ}|$-m_{JJ} grid. Fig. 5.10 shows the results.

Finally, picking the optimal $|\Delta\eta_{JJ}|$ and m_{JJ} cut combination, the maximum sensitivity is scaled to match various integrated luminosities. Fig. 5.11 shows the result. Trigger A and the 2015 trigger show approximately the same sensitivity. In the simulated events,[12] which are normalized to $9.99\,\text{fb}^{-1}$ of data, the 2015 trigger based selection results in 76 VBF H(bb) events in the signal region, while trigger A contributes with 42 events of the same sensitivity—an improvement of 55 %. Regarding trigger B, future studies will assess whether the forward region is affected by pileup jets that contribute to the background. If so, the sensitivity of

[12] In the simulated events the triggers are unprescaled.

trigger B is expected to increase once pileup mitigation techniques are employed for the forward region of the detector.

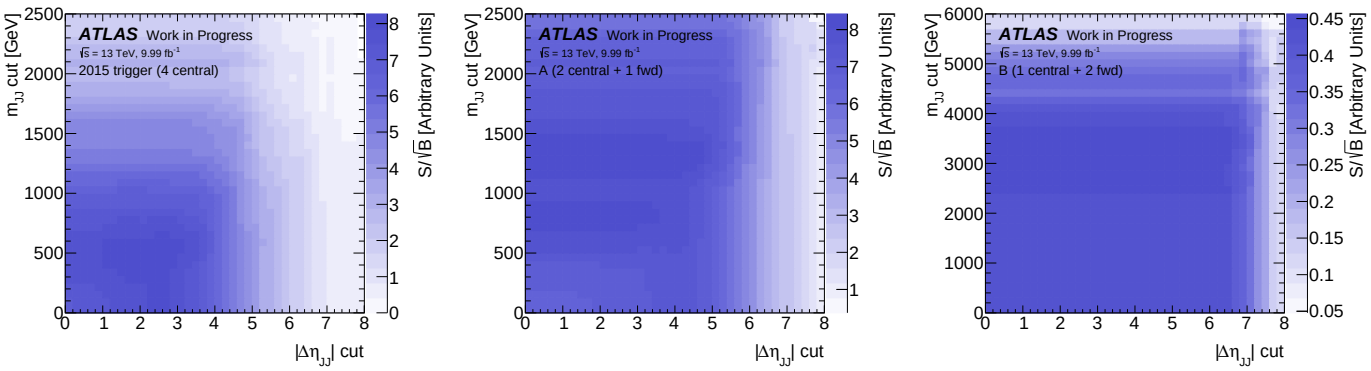

Figure 5.10.: Sensitivity of the studied triggers, evaluated for different $|\Delta\eta_{JJ}|$ and m_{JJ} cut combinations. The values on the axes refer to the respective quantity exceeding the value.

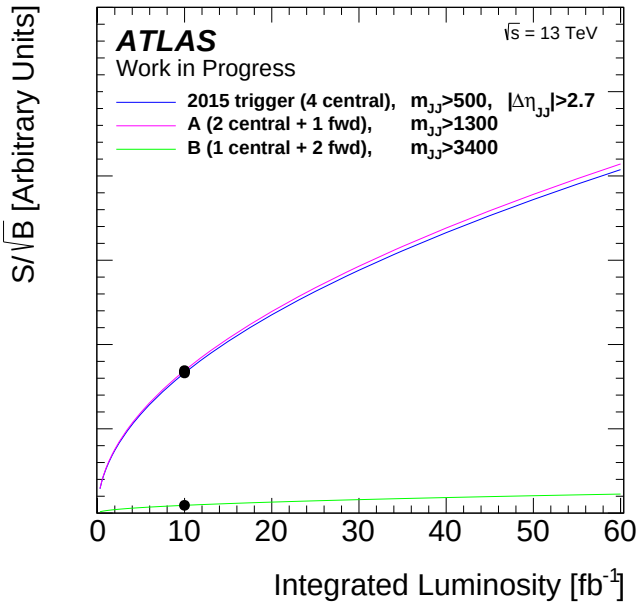

Figure 5.11.: Sensitivity evolution of the studied triggers. For each trigger, the optimal cut combination from Fig. 5.10 is picked and the resulting $S/\sqrt{B}$ is scaled for various integrated luminosities.

5.8. Further Developments

In this section, possible future improvements to the triggers are discussed. Sec. 5.8.1 contains a short study that is conducted in order to assess the viability of the L1Topo trigger C. Furthermore, the improvement of B via an OS requirement is mentioned. In Sec. 5.8.2, an alternative suggestion for the improvement of the HLT part of trigger B is given, in case its L1Topo improvement (OS) is not approved. Sec. 5.8.3 introduces improvements to the HLT parts of both triggers, A and B, that recently have been implemented into the data-taking trigger menu, replacing $\texttt{A}_{\text{HLT}}$ and $\texttt{B}_{\text{HLT}}$.

5.8.1. Topological Triggers at L1

The topological trigger C (whose L1 part is in this section referred to as `C`) that was conceived in Sec. 5.3 will be feasible with the trigger system upgrade L1Topo. Trigger C will serve as an alternative to a central multijet trigger like `L1_4J20` that is not affected by multijet inefficiencies. Tab. 5.6 shows a rudimentary study that is conducted in order to assess the potential of such a topological trigger. The achieved efficiencies seem promising but have to be carefully weighed against additional trigger rate. A more involved study is necessary to propose a concrete implementation.
Another quantity that L1Topo is able to trigger on is the highest invariant mass between jet RoIs (`INVM`). Since `DETA` and `INVM` are correlated, but not the same variable, a replacement of `DETA` with `INVM` should be considered in the study. Tab. 5.6 shows a similar performance of `DETA` and `INVM`.

Besides the introduction of a new trigger, L1Topo makes it possible to introduce an OS requirement for the forward jets of trigger `B`. Since events that have both forward jets on one side of the detector are mostly non-signal events, this requirement should not decrease the signal efficiency considerably. It should be introduced alongside a reduction of the E_T requirement of the central jet, to achieve a higher efficiency at the same rate.

Trigger	VBF H(bb) eff.	Raw rate [Hz]
L1_4J20	8.4 %	1410
L1_J40.0ETA25_2J25_J20.31ETA49 (= A)	14.6 %	2030
L1_J40.0ETA25_2J15.31ETA49 (= B)	4.5 %	270
L1_HT150-AJ20all.ETA30 _20DETA-AJ30all.ETA30-AJ20all.ETA30 (=: C1)	16.3 %	2670
L1_HT150-AJ20all.ETA30 _30DETA-AJ30all.ETA30-AJ20all.ETA30 (=: C2)	10.4 %	1200
L1_HT150-AJ20all.ETA30 _40DETA-AJ30all.ETA30-AJ20all.ETA30 (=: C3)	5.2 %	400
L1_HT150-AJ20all.ETA30 _400INVM-AJ30s6.ETA30-AJ20s6.ETA30 (=: C4)	9.2 %	1030
L1_HT150-AJ20all.ETA30 _600INVM-AJ30s6.ETA30-AJ20s6.ETA30 (=: C5)	4.5 %	350
L1_HT150-AJ20all.ETA30 _800INVM-AJ30s6.ETA30-AJ20s6.ETA30 (=: C6)	2.3 %	130
A ∨ B ∨ C1 ∨ L1_4J20	31.0 %	4670
A ∨ B ∨ C2 ∨ L1_4J20	28.1 %	3500
A ∨ B ∨ C3 ∨ L1_4J20	25.8 %	3000
A ∨ B ∨ C4 ∨ L1_4J20	27.9 %	3500
A ∨ B ∨ C5 ∨ L1_4J20	25.7 %	3000
A ∨ B ∨ C6 ∨ L1_4J20	24.7 %	2830

Table 5.6.: Exemplary L1 implementations of the topological trigger C, alongside the existing triggers. The rates of the variants of trigger C are estimates obtained using the method described in App. A.2.

5.8.2. Opposite Sides at HLT

Since the VBF H(bb) event topology does not usually feature two prominent forward jets in the same detector region (both forward or both backward), trigger B can be improved by adding an OS requirement to the HLT part—even without L1Topo. Fig. 5.12 shows how much the forward jets' p_T requirement at HLT level could be lowered while still using `L1_J40.0ETA25_2J15.31ETA49` at L1: The HLT threshold for the forward jets can be set to up to 35 GeV (Fig. 5.12b), while still having the trigger reach its plateau of efficiency with respect to an offline selection at 55 GeV (Fig. 5.12a).

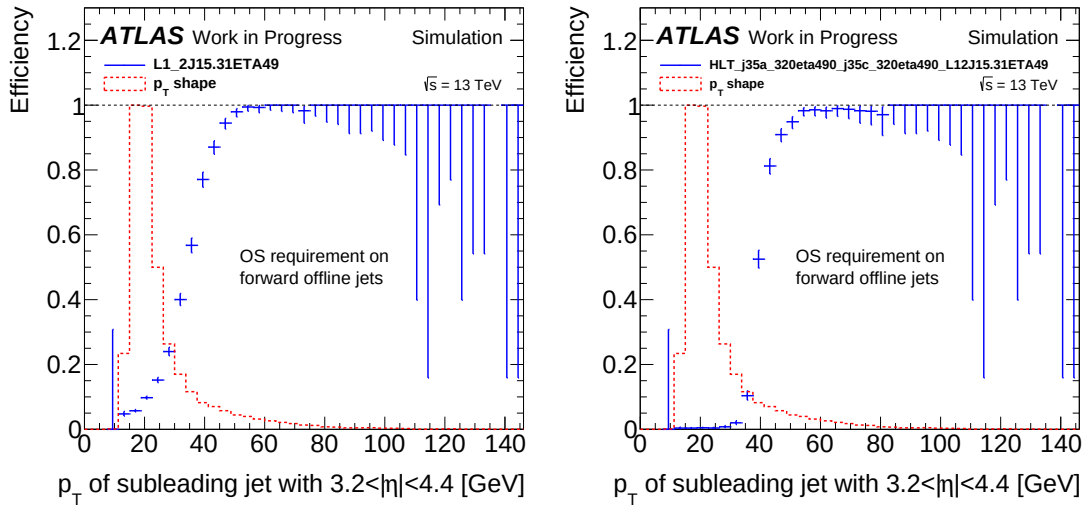

Figure 5.12.: Efficiency for the forward (a) L1 and (b) HLT part of trigger B, as a function of the subleading offline forward jet p_T. With respect to Fig. 5.4d and Fig. 5.5d, an OS requirement has been introduced at HLT and offline level. The p_T thresholds at offline and HLT level can be lowered significantly in this case.

5.8.3. Lower p_T Requirement on b-jets at HLT Level

The implemented HLT level triggers `HLT_j80_bmv2c2070_split_j60_bmv2c2085_split_j45_320eta490` and `HLT_j80_bmv2c2085_split_2j60_320eta490` require one jet with relatively high transverse momentum ($p_T > 80\,\text{GeV}$) and a b-tag. Fig. 5.13 illustrates a VBF H(bb) event topology that neither of those triggers would trigger on, since the b-tagging requirement is not satisfied by the $p_T = 80\,\text{GeV}$ jet. An attempt to also include these types of signal events in the trigger selection consists of requiring the b-tags independently of the p_T requirements. Tab. 5.7 shows the study that was conducted to assess the suitability of this approach.

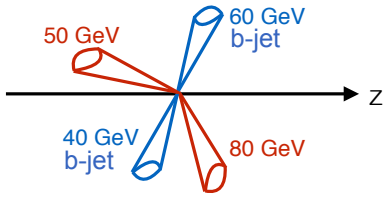

Figure 5.13.: VBF H(bb) event that would not be triggered on by the implemented HLT triggers.

The trigger

`HLT_j80_0eta240_j60_j45_320eta490_invm700_`
`AND_HLT_j45_bmv2c2070_split_j45_bmv2c2085_split`

as a replacement for

`HLT_j80_bmv2c2070_split_j60_bmv2c2085_split_j45_320eta490`

was proposed on April 28, 2016 [121]. Necessary changes in the trigger menu code were implemented by the ATLAS Trigger Menu group, to cope with this complicated trigger. Subsequently, obtained rate estimates made a less efficient b-tagging working point necessary. Additionally, it was found that trigger B can achieve low enough rates by dropping b-tagging requirements altogether, and introducing a requirement on the highest invariant mass between jets of the event.

The resulting replacement triggers for $\texttt{A}_{\text{HLT}}$ and $\texttt{B}_{\text{HLT}}$,

`HLT_j80_0eta240_j60_j45_320eta490_AND_2j45_bmv2c2070_split`,
eff. 1.92 %, raw rate 8.8 Hz, and
`HLT_j80_0eta240_2j60_320eta490_invm700`,
eff. 0.30 %, raw rate 4.2 Hz,

were implemented in the data-taking menu September 9, 2016.

Trigger	VBF H(bb) eff.	Uniq. rate [Hz]
HLT_j80_0eta240_j60_j45_320eta490_ AND_HLT_2j35_bmv2c2085_split	3.20 %	54
HLT_j80_0eta240_j60_j45_320eta490_ AND_HLT_2j45_bmv2c2085_split	2.71 %	46
HLT_j80_0eta240_j60_j45_320eta490_ AND_HLT_j35_bmv2c2070_split_j35_bmv2c2085_split	3.00 %	26
HLT_j80_0eta240_j60_j45_320eta490_ AND_HLT_j45_bmv2c2070_split_j45_bmv2c2085_split	2.52 %	23
HLT_j80_0eta240_j60_j45_320eta490_invm700_ AND_HLT_j45_bmv2c2070_split_j45_bmv2c2085_split	2.30 %	14
HLT_j80_0eta240_2j60_320eta490_invm700	0.30 %	2.6

Table 5.7.: Study on improved HLT triggers that require b-tags independently of high p_T jet kinematics. The non-b-jet part is the same for all triggers: HLT_j80_0eta240_j60_j45_320eta490. The respective L1 trigger is required to pass for all entries. The unique rate estimates are obtained using the method described in App. A.2.

6. Conclusions

There has not yet been an evidence for the Higgs boson decaying to beauty quarks. In particular, searches for a VBF produced Higgs boson decaying in this channel show a low sensitivity. This thesis has approached one of the main difficulties encountered in the ATLAS Run 1 search: the low trigger efficiency. The problem of a former focus on central jets was identified and according measures were adopted. Two triggers, specifically designed around the VBF H(bb) signature, and incorporating forward jets, were developed and implemented in the trigger menu.
The first requires two central jets, and one forward jet, while the second trigger requires one central, and two forward jets. A third trigger, which requires four central jets, and was implemented prior to the work of this thesis, continues to be included in the menu.
The performance of the new triggers was evaluated for both L1 and HLT, and compared against the third trigger. Combining the new triggers, the available statistics for the offline analysis increases by over 50 %. Furthermore, the first trigger reaches the same signal-to-noise ratio as the trigger requiring four central jets.
The problem of a low trigger efficiency continues to exists in Run 2, but the diminishing effect of the increased instantaneous luminosity on trigger efficiencies was damped.

Technologies that soon will be added to the ATLAS detector will enable the implementation of topological triggers at L1. From these, further increase of the available statistics is expected. The future trigger menu of the analysis will consist of the three mentioned triggers, along with the topological trigger.

The ATLAS Run 2 search for VBF H(bb) is ongoing and this thesis' work has

enhanced its sensitivity by allowing to record and analyze pp collision data that otherwise would not have been collected. Combining all production modes, an evidence of the Higgs boson decaying to $b\bar{b}$ is expected by the end of the LHC Run 2. Towards this goal, the VBF H(bb) analysis will contribute with its significance.

A. Appendix

A.1. Analysis Frameworks

A.1.1. Proposal Sections

The studies presented in Sec. 5.8 and Sec. 5.2 through 5.5 were conducted within the AnalysisBase 2.3.41 framework [122]. The toolset xAODAnaHelpers [123] (version `00-03-28`) was used for calibrating the `AntiKt4EMTopoJets` with the following configuration

```
CalibSequence JetArea_Residual_Origin_EtaJES_GSC
configNameAFII JES_Prerecommendation2015_AFII_Apr2015.config
configNameFullSim JES_MC15Prerecommendation_April2015.config
configNameData JES_MC15Prerecommendation_April2015.config
JESUncertConfig $ROOTCOREBIN/data/JetUncertainties/JES_2015/Prerec/
                                          PrerecJES2015_3NP_Scenario1_50ns.config
JESUncertMCType MC15
JERUncertConfig JetResolution/Prerec2015_xCalib_2012JER_ReducedTo9NP_Plots_v2.root
RedoJVT True
```

The dataset used for VBF H(bb) events in Sec. 5.8 and Sec. 5.2 through 5.5 is `mc15_13TeV.341566.PowhegPythia8EvtGen_CT10_AZNLOCTEQ6L1_VBFH125_bb.merge.AOD.e3988_a766_a767_r6264`.
Due to difficulties emulating b-jet triggers at HLT level, a workaround was used to compute the efficiencies presented in Tab. 5.2, 5.4, and 5.5: HLT jets are matched with the highest p_T offline jet found within $\Delta R < 0.3$ of the respective HLT jet. Then, the MV2c20 b-tagging weight of this matched offline jet is used as a b-tagging weight for the HLT jet. The offline working points [22] that correspond to b-jet efficiencies of 85 %, 77 %, and 70 %, respectively, were adjusted so that b-jet effi-

ciencies of 87 %, 79 %, and 72 % are reached at HLT level. The corresponding cuts on the MV2c20 discriminant were computed using a linear interpolation between the known working points.[1]

A.1.2. Data Sections

The studies presented in Sec. 5.6 and 5.7 were conducted within the CxAOD-Framework [124] (tag versions in `FrameworkSub-00-24-09`) which is based on the AnalysisBase 2.4.14 framework [122]. For the VBF H(bb) analysis, a new extension of the CxAODFramework was written [125].
The dataset used for VBF H(bb) events in Sec. 5.6 and 5.7 is
`mc15_13TeV.341566.PowhegPythia8EvtGen_CT10_AZNLOCTEQ6L1_VBFH125_bb.merge.DAOD_HIGG5D3.e3988_a766_a821_r7676_p2666`.

A.1.3. Further Development Section

The studies presented in Sec. 5.8.1 and 5.8.2 were conducted within the Framework discussed in App. A.1.1.
The efficiencies of the study presented in Sec. 5.8.3 were computed using a very early version of the `TrigBjetEmulation` tool [126], run on events of the dataset mentioned in App. A.1.1.

A.2. Rate Estimation

The rate estimates for L1 and HLT triggers that (*i*) were used in the process of coming up with the proposal presented in Sec. 5.4 and (*ii*) are quoted in Tab. 5.6 and 5.7 are computed with the `TrigRateFast` tool [127, 128]. It uses 13 TeV enhanced bias data extrapolated to an instantaneous luminosity of $2 \times 10^{34}\,\mathrm{cm}^{-2}\,\mathrm{s}^{-1}$. The rate for a given selection is calculated with the formula

$$\text{Rate [Hz]} = \alpha\, N(\zeta, w)/\Delta t,$$

[1] This results in the following MV2c20 cut values: loose (87% WP) cut: -0.835376, medium (79% WP) cut: -0.529846, tight (72% WP) cut: -0.143121.

where α is the ratio of the projected luminosity to the luminosity of the used data sample, $N(\zeta, w)$ is the weighted number of events satisfying selection ζ, and Δt is the length of the run of the data sample in seconds. The weight w of an event increases with the number of triggers fired in that event. The tool was used to validate the official[2] rate estimates of selected triggers and was found to be in good agreement.

As of the used version `00-00-03`, the tool does not support b-tagging at HLT level. For the triggers in Sec. 5.4 (whose unique rate estimates are not quoted in this thesis) and Tab. 5.7, a workaround was used: HLT jets are matched with the highest p_T offline jet found within $\Delta R < 0.3$ of the respective HLT jet. Then, the MV2c20 b-tagging weight of this matched offline jet is used as a b-tagging weight for the HLT jet. The cut values on the b-tagging weight that correspond to the b-tagging working points were gauged to make the tool match official rate estimations of selected b-jet triggers.[3]

Using the same workaround, a b-jet trigger menu with trigger requirements that are similar to the triggers listed in Tab. 5.7 was implemented in the tool. Against this menu, shown in Tab. A.1, the unique rates are given in Tab. 5.7.

[2] From the ATLAS Trigger Menu group.

[3] This method of determining the b-tagging weight cut values differs from the method described in App. A.1.1.

L1	HLT: jet and b-jet
J75.31ETA49	HLT_3j175
J100	HLT_4j100
J100.31ETA49	HLT_5j85
3J50	HLT_6j50_0eta240_L14J20
4J20	HLT_7j45_L14J20
5J15.0ETA25	HLT_ht1000_L1J100
6J15	HLT_2j75_bmedium_j75_L13J25.0ETA23
	HLT_2j55_bmedium_j100_L13J20_J75
	HLT_j75_bmedium_3j75_L14J20
	HLT_j70_btight_3j70_L14J20
	HLT_j175_bmedium_j60_bmedium_L1J100

Table A.1.: List of the L1 and HLT triggers that were implemented in the TrigRateFast tool to calculate unique rates.

Bibliography

[1] S. L. Glashow, *Partial-symmetries of weak interactions*, Nuclear Physics **22(4)**, 579 (1961), URL http://www.sciencedirect.com/science/article/pii/0029558261904692

[2] S. Weinberg, *A Model of Leptons*, Phys. Rev. Lett. **19**, 1264 (1967), URL http://link.aps.org/doi/10.1103/PhysRevLett.19.1264

[3] A. Salam, *Weak and Electromagnetic Interactions*, Conf.Proc. **C680519**, 367 (1968)

[4] H. Fritzsch, M. Gell-Mann, H. Leutwyler, *Advantages of the Color Octet Gluon Picture*, Phys. Lett. **B47**, 365 (1973)

[5] D. J. Gross, F. Wilczek, *Asymptotically Free Gauge Theories. 1*, Phys. Rev. **D8**, 3633 (1973)

[6] H. D. Politzer, *Asymptotic Freedom: An Approach to Strong Interactions*, Phys. Rept. **14**, 129 (1974)

[7] F. Englert, R. Brout, *Broken Symmetry and the Mass of Gauge Vector Mesons*, Phys. Rev. Lett. **13**, 321 (1964), URL http://link.aps.org/doi/10.1103/PhysRevLett.13.321

[8] P. W. Higgs, *Broken Symmetries and the Masses of Gauge Bosons*, Phys. Rev. Lett. **13**, 508 (1964), URL http://link.aps.org/doi/10.1103/PhysRevLett.13.508

[9] *SM Higgs production cross sections at* $\sqrt{s} = 13\,TeV$ *(update in CERN Report4 2016)*, https://twiki.cern.ch/twiki/bin/view/LHCPhysics/CERNYellowReportPageAt13TeV, version from July 2, 2016

[10] *NNLO+NNLL top-quark-pair cross sections*, `https://twiki.cern.ch/twiki/bin/view/LHCPhysics/TtbarNNLO`, version from September 14, 2015

[11] *Search for the Standard Model Higgs boson in $H \to \tau\tau$ decays in proton-proton collisions with the ATLAS detector*, Technical Report ATLAS-CONF-2012-160, CERN, Geneva (2012), URL `http://cds.cern.ch/record/1493624`

[12] K. Olive, et al. (Particle Data Group), *Review of Particle Physics*, Chin.Phys. **C38**, 090001 (2014)

[13] S. Heinemeyer, et al. (LHC Higgs Cross Section Working Group), *Handbook of LHC Higgs Cross Sections: 3. Higgs Properties* (2013), `1307.1347`

[14] M. Thomson, *Modern Particle Physics*, Cambridge University Press, United Kingdom (2013)

[15] R. Aaij, et al. (LHCb), *Observation of $J/\psi\phi$ structures consistent with exotic states from amplitude analysis of $B^+ \to J/\psi\phi K^+$ decays* (2016), `1606.07895`

[16] R. Aaij, et al. (LHCb), *Observation of $J/\psi p$ Resonances Consistent with Pentaquark States in $\Lambda_b^0 \to J/\psi K^- p$ Decays*, Phys. Rev. Lett. **115**, 072001 (2015), `1507.03414`

[17] D. W. Duke, J. F. Owens, *Q^2 Dependent Parametrizations of Parton Distribution Functions*, Phys. Rev. **D30**, 49 (1984)

[18] A. D. Martin, W. J. Stirling, R. S. Thorne, G. Watt, *Parton distributions for the LHC*, Eur. Phys. J. **C63**, 189 (2009), `0901.0002`

[19] M. Cacciari, G. P. Salam, G. Soyez, *The anti-k_t jet clustering algorithm*, JHEP **04**, 063 (2008), `0802.1189`

[20] P. Loch, S. Menke, P.-A. Delsart, C. J. Young, Z. Marshall, B. Axen, *Topological cell clustering in the ATLAS calorimeters and its performance in LHC Run I*, Technical Report ATL-COM-PHYS-2014-1439, CERN, Geneva (2014), URL `https://cds.cern.ch/record/1967028`

[21] G. Aad, et al. (ATLAS Collaboration), *Performance of b-Jet Identification in the ATLAS Experiment*, Technical Report CERN-PH-EP-2015-216. arXiv:1512.01094, CERN, Geneva (2015), URL `https://cds.cern.ch/record/2110203`

[22] *Expected performance of the ATLAS b-tagging algorithms in Run-2*, Technical Report ATL-PHYS-PUB-2015-022, CERN, Geneva (2015), URL `https://cds.cern.ch/record/2037697`

[23] G. Aad, et al. (ATLAS), *Measurements of the Higgs boson production and decay rates and coupling strengths using pp collision data at $\sqrt{s} = 7$ and 8 TeV in the ATLAS experiment*, Eur. Phys. J. **C76(1)**, 6 (2016), `1507.04548`

[24] V. Khachatryan, et al. (CMS), *Constraints on the Higgs boson width from off-shell production and decay to Z-boson pairs*, Phys. Lett. **B736**, 64 (2014), `1405.3455`

[25] V. Khachatryan, et al. (CMS), *Precise determination of the mass of the Higgs boson and tests of compatibility of its couplings with the standard model predictions using proton collisions at 7 and 8 TeV*, Eur. Phys. J. **C75(5)**, 212 (2015), `1412.8662`

[26] G. Aad, et al. (ATLAS), *Study of the spin and parity of the Higgs boson in diboson decays with the ATLAS detector*, Eur. Phys. J. **C75(10)**, 476 (2015), [Erratum: Eur. Phys. J.C76,no.3,152(2016)], `1506.05669`

[27] V. Khachatryan, et al. (CMS), *Constraints on the spin-parity and anomalous HVV couplings of the Higgs boson in proton collisions at 7 and 8 TeV*, Phys. Rev. **D92(1)**, 012004 (2015), `1411.3441`

[28] G. Aad, et al. (ATLAS), *Evidence for the Higgs-boson Yukawa coupling to tau leptons with the ATLAS detector*, JHEP **04**, 117 (2015), `1501.04943`

[29] S. Chatrchyan, et al. (CMS), *Evidence for the 125 GeV Higgs boson decaying to a pair of τ leptons*, JHEP **05**, 104 (2014), `1401.5041`

[30] J. M. Campbell, J. W. Huston, W. J. Stirling, *Hard Interactions of Quarks and Gluons: A Primer for LHC Physics*, Rept. Prog. Phys. **70**, 89 (2007), `hep-ph/0611148`

[31] The ATLAS collaboration (ATLAS), *Measurement of inclusive-jet cross-sections in proton-proton collisions at* $\sqrt{s} = 13$ TeV *centre-of-mass energy with the ATLAS detector* (2016)

[32] F. Wilczek, *Decays of Heavy Vector Mesons Into Higgs Particles*, Phys. Rev. Lett. **39**, 1304 (1977)

[33] H. M. Georgi, S. L. Glashow, M. E. Machacek, D. V. Nanopoulos, *Higgs Bosons from Two Gluon Annihilation in Proton Proton Collisions*, Phys. Rev. Lett. **40**, 692 (1978)

[34] E. Eichten, I. Hinchliffe, K. D. Lane, C. Quigg, *Super Collider Physics*, Rev. Mod. Phys. **56**, 579 (1984), [Addendum: Rev. Mod. Phys.58,1065(1986)]

[35] S. Dawson, *Radiative corrections to Higgs boson production*, Nucl. Phys. **B359**, 283 (1991)

[36] A. Djouadi, M. Spira, P. M. Zerwas, *Production of Higgs bosons in proton colliders: QCD corrections*, Phys. Lett. **B264**, 440 (1991)

[37] M. Spira, A. Djouadi, D. Graudenz, P. M. Zerwas, *Higgs boson production at the LHC*, Nucl. Phys. **B453**, 17 (1995), `hep-ph/9504378`

[38] A. Stange, W. J. Marciano, S. Willenbrock, *Associated production of Higgs and weak bosons, with* $H \to b\bar{b}$*, at hadron colliders*, Phys. Rev. **D50**, 4491 (1994), `hep-ph/9404247`

[39] J. R. Ellis, M. K. Gaillard, D. V. Nanopoulos, *A Phenomenological Profile of the Higgs Boson*, Nucl. Phys. **B106**, 292 (1976)

[40] S. L. Glashow, D. V. Nanopoulos, A. Yildiz, *Associated Production of Higgs Bosons and Z Particles*, Phys. Rev. **D18**, 1724 (1978)

[41] E. Ma, J. Okada, *Possible Means of Detecting the Higgs Boson in e^+e^- Annihilation*, Phys. Rev. **D20**, 1052 (1979)

[42] F. Abe, et al. (CDF), *A Limit on the top quark mass from $p\bar{p}$ collisions at $\sqrt{s} = 1.8$ TeV*, Phys. Rev. **D45**, 3921 (1992)

[43] V. D. Barger, F. Halzen, W.-Y. Keung, *A New Higgs Trigger in e^+e^- Collisions*, Phys. Lett. **B110**, 323 (1982), [Erratum: Phys. Lett.B117,467(1982)]

[44] D. A. Dicus, S. S. D. Willenbrock, *Higgs Bosons From Vector Boson Fusion in e^+e^-, ep and pp Collisions*, Phys. Rev. **D32**, 1642 (1985)

[45] C. H. Haber, et al., *The CDF SVX: A silicon vertex detector for a hadron collider*, Nucl. Instrum. Meth. **A289**, 388 (1990)

[46] A. Stange, W. J. Marciano, S. Willenbrock, *Higgs bosons at the Fermilab Tevatron*, Phys. Rev. **D49**, 1354 (1994), `hep-ph/9309294`

[47] D. Froidevaux, E. Richter-Was, *Is the channel $H \to b\bar{b}$ observable at LHC?*, Z. Phys. **C67**, 213 (1995)

[48] B. Mours, et al., *The Design, construction and performance of the ALEPH silicon vertex detector*, Nucl. Instrum. Meth. **A379**, 101 (1996)

[49] P. P. Allport, et al. (OPAL), *The OPAL silicon microvertex detector*, Nucl. Instrum. Meth. **A324**, 34 (1993)

[50] N. Bingefors, et al., *The DELPHI microvertex detector*, Nucl. Instrum. Meth. **A328**, 447 (1993)

[51] M. Acciarri, et al. (L3 SMD), *The L3 silicon microvertex detector*, Nucl. Instrum. Meth. **A351**, 300 (1994)

[52] R. Barate, et al. (LEP Working Group for Higgs boson searches, ALEPH, DELPHI, L3, OPAL), *Search for the standard model Higgs boson at LEP*, Phys.Lett. **B565**, 61 (2003), `hep-ex/0306033`

[53] F. Abe, et al. (CDF), *Search for new particles decaying into $b\bar{b}$ and produced in association with W bosons decaying into $e\nu$ or $\mu\nu$ at the Tevatron*, Phys. Rev. Lett. **79**, 3819 (1997)

[54] F. Abe, et al. (CDF), *Search for Higgs bosons produced in association with a vector boson in $p\bar{p}$ collisions at $\sqrt{s} = 1.8$ TeV*, Phys. Rev. Lett. **81**, 5748 (1998)

[55] T. Aaltonen, et al. (CDF, D0), *Evidence for a particle produced in association with weak bosons and decaying to a bottom-antibottom quark pair in Higgs boson searches at the Tevatron*, Phys.Rev.Lett. **109**, 071804 (2012), 1207.6436

[56] G. Aad, et al. (ATLAS), *Search for the $b\bar{b}$ decay of the Standard Model Higgs boson in associated $(W/Z)H$ production with the ATLAS detector*, JHEP **01**, 069 (2015), 1409.6212

[57] S. Chatrchyan, et al. (CMS), *Search for the standard model Higgs boson produced in association with a W or a Z boson and decaying to bottom quarks*, Phys.Rev. **D89(1)**, 012003 (2014), 1310.3687

[58] B. A. Dobrescu, K. Kong, R. Mahbubani, *Prospects for top-prime quark discovery at the Tevatron*, JHEP **06**, 001 (2009), 0902.0792

[59] R. Raitio, W. W. Wada, *Higgs Boson Production at Large Transverse Momentum in QCD*, Phys. Rev. **D19**, 941 (1979)

[60] J. N. Ng, P. Zakarauskas, *A QCD Parton Calculation of Conjoined Production of Higgs Bosons and Heavy Flavors in $p\bar{p}$ Collision*, Phys. Rev. **D29**, 876 (1984)

[61] W. J. Marciano, F. E. Paige, *Associated production of Higgs bosons with t anti-t pairs*, Phys. Rev. Lett. **66**, 2433 (1991)

[62] D. Decamp, et al. (ALEPH), *Searches for the standard Higgs boson*, Phys. Lett. **B246**, 306 (1990)

[63] J. F. Gunion, *Associated top anti-top Higgs production as a large source of WH events: Implications for Higgs detection in the $\ell\nu\gamma\gamma$ final state*, Phys. Lett. **B261**, 510 (1991)

[64] P. Bock, et al. (DELPHI, OPAL, ALEPH, L3), *Searches for Higgs bosons: Preliminary combined results from the four LEP experiments at $\sqrt{s} \approx 189$ GeV*, in *Proceedings, International Europhysics Conference on High energy physics (EPS-HEP 1999): Tampere, Finland, July 15-21, 1999* (1999), URL `http://alice.cern.ch/format/showfull?sysnb=0339313`

[65] A. Airapetian, et al. (ATLAS), *ATLAS: Detector and physics performance technical design report. Volume 2* (1999)

[66] S. Dawson, L. Reina, *Associated top Higgs production at future colliders*, Int. J. Mod. Phys. **A16S1A**, 375 (2001), `hep-ph/0011290`

[67] S. Dawson, C. Jackson, L. H. Orr, L. Reina, D. Wackeroth, *Associated Higgs production with top quarks at the large hadron collider: NLO QCD corrections*, Phys. Rev. **D68**, 034022 (2003), `hep-ph/0305087`

[68] S. Lai, *Search for Standard Model Higgs Boson Produced in Association with a Top Anti-top Quark Pair in 1.96 TeV Proton - Anti-proton Collisions*, Ph.D. thesis, Toronto U. (2007), URL `http://lss.fnal.gov/archive/thesis/2000/fermilab-thesis-2007-92.pdf`

[69] The DØ Collaboration (D0), *Search for the Standard Model Higgs boson in the $t\bar{t}H \to t\bar{t}b\bar{b}$ channel*, in *Preliminary Results for Summer 2008 Conferences* (2008), URL `http://www-d0.fnal.gov/Run2Physics/WWW/results/prelim/HIGGS/H58/`

[70] J. P. Agnew, *Search for the Associate Production of Higgs Bosons with Top Anti-Top Pairs.*, Ph.D. thesis, Manchester U. (2014), URL `http://lss.fnal.gov/archive/thesis/2000/fermilab-thesis-2014-09.shtml`

[71] T. Aaltonen, et al. (CDF), *Search for the standard model Higgs boson produced in association with top quarks using the full CDF data set*, Phys. Rev. Lett. **109**, 181802 (2012), `1208.2662`

[72] G. Aad, et al. (ATLAS), *Search for the Standard Model Higgs boson produced in association with top quarks and decaying into $b\bar{b}$ in pp collisions at $\sqrt{s}$ = 8 TeV with the ATLAS detector*, Eur. Phys. J. **C75(7)**, 349 (2015), 1503.05066

[73] V. Khachatryan, et al. (CMS), *Search for the associated production of the Higgs boson with a top-quark pair*, JHEP **09**, 087 (2014), [Erratum: JHEP10,106(2014)], 1408.1682

[74] V. Khachatryan, et al. (CMS), *Search for a Standard Model Higgs Boson Produced in Association with a Top-Quark Pair and Decaying to Bottom Quarks Using a Matrix Element Method*, Eur. Phys. J. **C75(6)**, 251 (2015), 1502.02485

[75] G. Aad, et al. (ATLAS), *Search for the Standard Model Higgs boson decaying into $b\bar{b}$ produced in association with top quarks decaying hadronically in pp collisions at $\sqrt{s} = 8$ TeV with the ATLAS detector*, JHEP **05**, 160 (2016), 1604.03812

[76] D. R. T. Jones, S. T. Petcov, *Heavy Higgs Bosons at LEP*, Phys. Lett. **B84**, 440 (1979)

[77] G. Barbiellini, G. Bonneaud, G. Coignet, J. R. Ellis, M. K. Gaillard, J. F. Grivaz, C. Matteuzzi, B. H. Wiik, *The production and detection of Higgs particles at LEP* (1979)

[78] R. N. Cahn, S. Dawson, *Production of Very Massive Higgs Bosons*, Phys. Lett. **B136**, 196 (1984), [Erratum: Phys. Lett.B138,464(1984)]

[79] R. N. Cahn, *Production of Heavy Higgs Bosons: Comparisons of Exact and Approximate Results*, Nucl. Phys. **B255**, 341 (1985), [Erratum: Nucl. Phys.B262,744(1985)]

[80] R. N. Cahn, S. D. Ellis, R. Kleiss, W. J. Stirling, *Transverse Momentum Signatures for Heavy Higgs Bosons*, Phys. Rev. **D35**, 1626 (1987)

[81] V. D. Barger, K.-m. Cheung, T. Han, J. Ohnemus, D. Zeppenfeld, *A Comparative study of the benefits of forward jet tagging in heavy Higgs production at the SSC*, Phys. Rev. **D44**, 1426 (1991)

[82] G. Grindhammer, D. Haidt, J. Ohnemus, J. Vermaseren, D. Zeppenfeld, *Searching for the Higgs in e p collisions at LEP / LHC*, in *ECFA Large Hadron Collider (LHC) Workshop: Physics and Instrumentation Aachen, Germany, October 4-9, 1990*, pages 0967–985 (1990), URL `http://alice.cern.ch/format/showfull?sysnb=0129347`

[83] M. van der Horst, K. J. F. Gaemers, R. M. Godbole, *The production of $W^{\pm}$, Z^0 vector bosons and Higgs bosons at the HERA collider*, in *DESY Workshop 1987: Physics at HERA Hamburg, Germany, October 12-14, 1987*, pages 739–769 (1987)

[84] M. Krawczyk, *Higgs search at HERA*, in *Future physics with light and heavy nuclei at HERMES. Contributions to the proceedings of the '95 - '96 Workshop on Future Physics at HERA, working group on light and heavy nuclei at HERA. Part 2* (1996), `hep-ph/9609477`

[85] V. A. Khoze, A. D. Martin, M. G. Ryskin, *High p_T Higgs signal for the LHC*, Eur. Phys. J. **C21**, 99 (2001), `hep-ph/0104230`

[86] A. De Roeck, V. A. Khoze, A. D. Martin, R. Orava, M. G. Ryskin, *Ways to detect a light Higgs boson at the LHC*, Eur. Phys. J. **C25**, 391 (2002), `hep-ph/0207042`

[87] M. L. Mangano, M. Moretti, F. Piccinini, R. Pittau, A. D. Polosa, *$b\bar{b}$ final states in Higgs production via weak boson fusion at the LHC*, Phys. Lett. **B556**, 50 (2003), `hep-ph/0210261`

[88] V. A. Khoze, M. G. Ryskin, W. J. Stirling, P. H. Williams, *A Z monitor to calibrate Higgs production via vector boson fusion with rapidity gaps at the LHC*, Eur. Phys. J. **C26**, 429 (2003), `hep-ph/0207365`

[89] M. Ciccolini, A. Denner, S. Dittmaier, *Electroweak and QCD corrections to Higgs production via vector-boson fusion at the LHC*, Phys. Rev. **D77**, 013002 (2008), 0710.4749

[90] P. Nason, C. Oleari, *NLO Higgs boson production via vector-boson fusion matched with shower in POWHEG*, JHEP **02**, 037 (2010), 0911.5299

[91] P. Bolzoni, F. Maltoni, S.-O. Moch, M. Zaro, *Higgs production via vector-boson fusion at NNLO in QCD*, Phys. Rev. Lett. **105**, 011801 (2010), 1003.4451

[92] M. Aaboud, et al. (ATLAS), *Search for the Standard Model Higgs boson produced by vector-boson fusion in 8 TeV pp collisions and decaying to bottom quarks with the ATLAS detector* (2016), 1606.02181

[93] V. Khachatryan, et al. (CMS), *Search for the standard model Higgs boson produced through vector boson fusion and decaying to $b\bar{b}$*, Phys. Rev. **D92(3)**, 032008 (2015), 1506.01010

[94] F. Ahmadov, et al., *Supporting Document for the Search for the bb decay of the Standard Model Higgs boson in associated (W/Z)H production with the ATLAS detector*, Technical Report ATL-COM-PHYS-2014-051, CERN, Geneva (2014), URL https://cds.cern.ch/record/1645654

[95] E. Gabrielli, F. Maltoni, B. Mele, M. Moretti, F. Piccinini, R. Pittau, *Higgs Boson Production in Association with a Photon in Vector Boson Fusion at the LHC*, Nucl. Phys. **B781**, 64 (2007), hep-ph/0702119

[96] T. L. Lungov, C. O. Escobar, *Using rapidity gaps to distinguish between Higgs production by W and gluon fusion*, Phys. Rev. **D53**, 4857 (1996), hep-ph/9510209

[97] J. D. Bjorken, *Rapidity gaps and jets as a new physics signature in very high-energy hadron hadron collisions*, Phys. Rev. **D47**, 101 (1993)

[98] E. Gotsman, E. M. Levin, U. Maor, *Large rapidity gaps in pp collisions*, Phys. Lett. **B309**, 199 (1993), hep-ph/9302248

[99] C. Collaboration (CMS), *Performance of quark/gluon discrimination in 8 TeV pp data* (2013)

[100] J. Gallicchio, M. D. Schwartz, *Seeing in Color: Jet Superstructure*, Phys. Rev. Lett. **105**, 022001 (2010), 1001.5027

[101] V. Khachatryan, et al. (CMS), *CMS Tracking Performance Results from early LHC Operation*, Eur. Phys. J. **C70**, 1165 (2010), 1007.1988

[102] L. Evans, P. Bryant, *LHC Machine*, Journal of Instrumentation **3(08)**, S08001 (2008), URL http://stacks.iop.org/1748-0221/3/i=08/a=S08001

[103] G. Aad, et al. (ATLAS), *The ATLAS Experiment at the CERN Large Hadron Collider*, JINST **3**, S08003 (2008)

[104] A. Artamonov, et al., *The ATLAS forward calorimeters*, JINST **3**, P02010 (2008)

[105] G. Aad, et al. (ATLAS), *Topological cell clustering in the ATLAS calorimeters and its performance in LHC Run 1* (2016), 1603.02934

[106] G. Aad, et al. (ATLAS Collaboration), *Technical Design Report for the Phase-I Upgrade of the ATLAS TDAQ System*, Technical Report CERN-LHCC-2013-018. ATLAS-TDR-023, CERN, Geneva (2013), final version presented to December 2013 LHCC., URL https://cds.cern.ch/record/1602235

[107] E. Simioni, et al., *Upgrade of the ATLAS Level-1 Trigger with event topology information*, J. Phys. Conf. Ser. **664(8)**, 082052 (2015)

[108] T. Berger-Hryn'ova, R. Caputo, K. Nagano, C. Ohm, *Physics Uses and Hardware Constraints of the L1 Topological Trigger*, Technical Report ATL-COM-DAQ-2014-005, CERN, Geneva (2014), URL https://cds.cern.ch/record/1645921

[109] R. Achenbach, et al., *The ATLAS level-1 calorimeter trigger*, JINST **3**, P03001 (2008)

[110] Hryn'ova, T and Nagano, K, *Trigger Menu Strategy for Run 2*, Technical Report ATL-COM-DAQ-2014-054, CERN, Geneva (2014), URL `https://cds.cern.ch/record/1703730`

[111] *Trigger Naming Run 2*, `https://twiki.cern.ch/twiki/bin/view/Atlas/TriggerNamingRun2`, version from November 30, 2015

[112] *Updated allowed L1 eta range values*, `https://its.cern.ch/jira/browse/ATR-11526`, version from June 24, 2015

[113] A. Favareto, E. Guido, Y.-K. Kim, K. Krizka, Y. Okumura, F. Parodi, L. P. Rossi, C. Schiavi, C. Varni, *Search for the Standard Model Higgs boson produced by vector boson fusion and decaying to beauty quarks with the ATLAS detector*, Technical Report ATL-COM-PHYS-2014-1430, CERN, Geneva (2014), URL `https://cds.cern.ch/record/1966670`

[114] *Run I Jet Trigger Nomenclature and Conventions*, `https://twiki.cern.ch/twiki/bin/view/Atlas/TrigJetMenuRunI`, version from October 1, 2014

[115] *b-Jet trigger working points*, `https://twiki.cern.ch/twiki/bin/view/Atlas/TrigBjetWorkingPoints`, version from November 1, 2012

[116] *Jet menu from Period I of the ATLAS 2012 run*, `https://atlas-trigconf.cern.ch/run1/smkey/1514/l1key/9454/hltkey/7501/#JetTauEtmiss`, visited on March 23, 2016

[117] *Lowest un-prescaled triggers per data-taking period*, `https://twiki.cern.ch/twiki/bin/view/Atlas/LowestUnprescaled`, version from February 26, 2016

[118] *Proposal for 2015 b-jet trigger menu*, `https://twiki.cern.ch/twiki/bin/view/Atlas/TrigBjetMenu2015`, version from February 25, 2016

[119] *ATLAS Run Queries*, `https://atlas-runquery.cern.ch`, visited on September 19, 2016

[120] The ATLAS collaboration (ATLAS), *Tagging and suppression of pileup jets* (2014)

[121] *Higgs: H(bb) VBF trigger proposal*, https://its.cern.ch/jira/browse/ATR-13526, version from September 9, 2016

[122] *AnalysisBase*, https://twiki.cern.ch/twiki/bin/view/AtlasProtected/AnalysisBase, visited on September 19, 2016

[123] *xAODAnaHelpers Documentation*, https://xaodanahelpers.readthedocs.org/, visited on September 19, 2016

[124] *Twiki of the CxAODFramework*, https://twiki.cern.ch/twiki/bin/view/AtlasProtected/CxAODFramework, version from August 8, 2016

[125] *Twiki of the ATLAS Run 2 VBF H(bb) analysis*, https://twiki.cern.ch/twiki/bin/view/AtlasProtected/HSG5RunIIVBFHbb, version from September 9, 2016

[126] *Emulation tool for b-jet triggers*, https://twiki.cern.ch/twiki/bin/view/Atlas/TrigBjetEmulation, version from April 14, 2016

[127] *TrigRateFast*, https://twiki.cern.ch/twiki/bin/view/Atlas/TriggerRateEstimateTools, version from January 20, 2016

[128] *Rate estimation with 13 TeV data: a new tool*, https://indico.cern.ch/event/485230/contribution/78/attachments/1214428/1772793/RateEstimate_Carlson_Jan20-2015.pdf, visited on September 19, 2016; talk from January 20, 2015

Acknowledgments

I would like to express my gratitude to my advisor Francesco Rubbo who has, throughout the course of this thesis, given me advice, answered all the questions I had, was available at the most unconventional times, and whom I had many fruitful discussions with. From suggesting me this topic to work on, via the warm welcome in your group, through to your great enthusiasm and appreciating words for my work, I thank you very much, Ariel Schwartzman. My time in California was wonderful and I most sincerely thank Arnulf Quadt and Su Dong who made this connection, from Göttingen to SLAC, which was a first, possible.
Last and the most I thank my parents for their support throughout my studies.

Erklärung nach §17(9) der Prüfungsordnung für den Bachelor-Studiengang Physik und den Master-Studiengang Physik an der Universität Göttingen:

Hiermit erkläre ich, dass ich diese Abschlussarbeit selbständig verfasst habe, keine anderen als die angegebenen Quellen und Hilfsmittel benutzt habe und alle Stellen, die wörtlich oder sinngemäß aus veröffentlichten Schriften entnommen wurden, als solche kenntlich gemacht habe.
Darüberhinaus erkläre ich, dass diese Abschlussarbeit nicht, auch nicht auszugsweise, im Rahmen einer nichtbestandenen Prüfung an dieser oder einer anderen Hochschule eingereicht wurde.

Göttingen, den 5. Februar 2017

(Fabian Kukuck)